

**A Phenomenological Model of  
Scintillation of Infrared Radiation  
from Point Targets over Water and  
Measurements of the Model  
Parameters**

R. C. Warren

DSTO-RR-0231

**DISTRIBUTION STATEMENT A**  
Approved for Public Release  
Distribution Unlimited

20020815 190

# A Phenomenological Model of Scintillation of Infrared Radiation from Point Targets over Water and Measurements of the Model Parameters

*R. C. Warren*

**Weapons Systems Division  
Aeronautical and Maritime Research Laboratory**

DSTO-RR-0231

## ABSTRACT

As part of a study of the long range detection of antiship missiles (ASMs) by infrared search and track (IRST) systems using staring sensors, measurements of scintillation of an infrared source have been made. Scintillation of IR radiation from ASMs is one of a few features which may enhance ASM detectability by IRST systems. The measurements were made in the 3-5 micron band at ranges of 17 km and 19.9 km over water. The data were used to provide values for parameters of a phenomenological model of scintillation for use in development of detection algorithms. The parameters were the magnitude of irradiance, blurring effects and image location, and the correlation coefficients of these parameters. It was found that the probability distribution for the irradiance fluctuations was log-Gaussian, as predicted by theory. There was a temporal correlation for each of the parameters which was quantified by a correlation time, but none of the parameters were correlated with any other. Approximate methods were developed for correcting the data for the finite pixel size effects of the camera and the blurring effect of the optics.

## RELEASE LIMITATION

*Approved for public release*

*Published by*

*DSTO Aeronautical and Maritime Research Laboratory  
506 Lorimer St  
Fishermans Bend, Victoria 3207 Australia*

*Telephone: (03) 9626 7000  
Fax: (03) 9626 7999  
© Commonwealth of Australia 2002  
AR-012-166  
January 2002*

**APPROVED FOR PUBLIC RELEASE**

# A Phenomenological Model of Scintillation of Infrared Radiation from Point Targets over Water and Measurements of the Model Parameters

## Executive Summary

Infrared search and track (IRST) systems have been developed to improve the capability of surface ships to detect the approach of anti-ship sea-skimming missiles (ASMs). Current generation systems are based on a scanning sensor with update rates of the order of 1 Hz. The scanning method limits the time spent at any one pixel to the order of microseconds, which gives a low signal level and a poor signal-noise ratio. The next generation systems will be based on staring sensors, which will have much longer integration times and higher update rates, and so will have a considerable increase in detection and tracking capability.

The aim is to detect an incoming missile as soon as it appears over the horizon. Under these conditions the ASM appears as a very dim stationary point object which is extremely difficult to detect. There are few features of targets in IRST images that can be used as discriminators between true targets and false alarms. One feature is scintillation. The propagation environment near the sea surface is very complex. In particular there are refraction effects caused by refractive index gradients due to temperature gradients at the sea surface. Random fluctuations in the refractive index caused by turbulence lead to scintillation of distant point sources. The next generation of staring IRSTs will operate at frame rates sufficiently high to be able to exploit these effects.

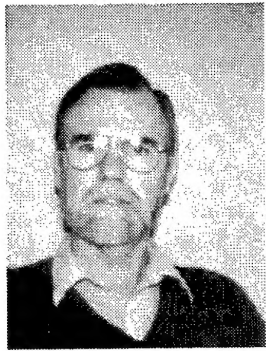
Target detection involves some form of spatial and/or temporal image filtering to enhance the response of targets and reduce the effect of clutter. Usually a thresholding operation is performed to isolate the brightest pixels as possible targets. These possible target locations are then passed to a tracker which establishes target tracks and can reject tracks showing non-targetlike behaviour. In order to develop and test detection and tracking algorithms for IRST systems it is necessary to have representative image sequences of the target of interest in the range of backgrounds encountered in service. The collection of real image sequences for all the situations required would be a considerable task. A practical alternative is to generate synthetic image sequences based on mathematical models of the target and background. Synthetic targets could be placed in images of real backgrounds, or realistic backgrounds could be generated using modelling tools. The insertion of synthetic targets is a complex problem. As well as atmospheric absorption of the target emissions and radiance along the target line of sight, atmospheric turbulence and sensor effects must be modelled. Currently the effect

of scintillation generated by atmospheric turbulence not sufficiently understood to allow accurate target modelling from first principles.

This paper proposes a phenomenological model of scintillation which would allow the generation of synthetic target images with sufficient accuracy for algorithm development. The parameters of the model are the maximum intensity, blurring and location of images of scintillating point targets. To obtain data for the model, measurements were made of the effect of atmospheric turbulence on the transmission of 3-5  $\mu\text{m}$  IR over a path of approximately 20 km over water. An Amber Galileo IR camera with a 300 mm lens was used as a sensor.

The data were processed to correct for the sensor effects and to extract the intrinsic parameters describing scintillation. Conclusions are drawn for the selection of design parameters for staring IRST systems. Suggestions are made for improvements to the design of the experiments to improve the accuracy of the derived parameters.

## Authors



**R. C. Warren**  
Weapons Systems Division

*Before joining DSTO in 1968, Bob Warren undertook research in the fields of X-ray and neutron diffraction and X-ray spectroscopy. At DSTO Salisbury he studied the mechanical properties of composite and nitrocellulose propellants, and he made significant contributions to the understanding of molecular relaxations in nitrocellulose. After a 2 year attachment in the UK, he made a number of discoveries in the rheology of nitrocellulose propellants. After working on the modelling and measurement of IR emissions from rocket exhaust plumes, he is now conducting research into the improvement of the performance of IR search and track systems.*

---

# Contents

1. INTRODUCTION .....	1
2. SCINTILLATION.....	3
2.1 Standard theory .....	3
2.2 Previous Measurements .....	5
2.3 Phenomenological model.....	7
2.4 Effect of finite sensor size on imaging of point sources .....	9
3. EXPERIMENTAL.....	10
3.1 Site location.....	10
3.2 Source.....	10
3.3 IR sensor.....	10
3.4 Meteorological conditions .....	11
3.5 Data file codes .....	11
4. RESULTS .....	12
4.1 Data analysis.....	12
4.2 Calibration .....	12
4.3 Registration and background subtraction.....	12
4.4 Magnitude of apparent scintillation in the raw data .....	13
4.5 Temporal correlation of observed signal magnitudes.....	15
4.6 Effect of attenuators .....	16
5. DISCUSSION.....	17
5.1 Corrected radiance maxima and point spread functions.....	17
5.2 Effect of finite pixel size.....	19
5.3 Point spread functions of the optics and atmosphere.....	20
5.4 Temporal correlation of PSF width .....	21
5.5 Image motion due to scintillation.....	21
5.6 Temporal correlation of image location .....	22
5.7 Correlations between parameters .....	23
5.8 Absolute values of parameters .....	25
5.9 Effect of meteorological conditions.....	26
5.10 Consequences of scintillation and atmospheric blurring for IRST systems	27
6. CONCLUSIONS.....	28
7. ACKNOWLEDGEMENTS.....	29
8. REFERENCES.....	29
APPENDIX A: SITE MAP .....	33
APPENDIX B: METEOROLOGICAL CONDITIONS.....	35
APPENDIX C: DATA RECORDING DETAILS .....	37
APPENDIX D: PARAMETERS OF RAW RADIANCE DISTRIBUTIONS.....	39

APPENDIX E: CORRELATION TIMES OF RADIANCE FLUCTUATIONS .....	41
APPENDIX F: CALCULATION OF THE EFFECTS OF FINITE PIXEL SIZE.....	43
APPENDIX G: POINT SPREAD FUNCTIONS OF THE OPTICS AND ATMOSPHERE .....	51
APPENDIX H: CORRELATIONS BETWEEN PARAMETERS .....	53

## 1. Introduction

Infrared search and track (IRST) systems have been developed to improve the capability of surface ships to detect the approach of anti-ship sea-skimming missiles (ASMs). Current generation systems are based on scanning sensors with update rates of the order of 1 Hz. The scanning method limits the time spent at any one pixel to the order of microseconds, which gives a low signal level and a poor signal-noise ratio. The next generation systems will be based on staring sensors, which will have much longer integration times and higher update rates, and so will have a considerable increase in detection and tracking capability.

The aim of IRST used for ASM defence is to detect an incoming missile as soon as it appears over the horizon. Under these conditions the sea-skimming ASM appears as a very dim stationary object which is extremely difficult to detect. Its intensity may be too weak to provide a basis for detection and the fact that it appears to be stationary makes it blend with the background. Many point detection algorithms rely on target motion for detection and assume that stationary objects belong to the background. There are few features that can act as discriminators between targets and false alarms. One possibility is the difference in response in the two IR bands 3-5  $\mu\text{m}$  and 8-12  $\mu\text{m}$ . However, in the tropical environments often found around Australia the transmission in the 8-12  $\mu\text{m}$  band is too poor for its use in detection. It is possible to use two colours within the 3-5 $\mu\text{m}$  band. However, such systems are not yet available and this effect will not be considered here.

A feature which would aid ASM detection is scintillation. The propagation environment near the sea surface is very complex. As well as the molecular absorption present in the general atmosphere, there are aerosol effects caused by particles generated from breaking waves, and refraction effects caused by refractive index gradients due to temperature gradients at the sea surface. Random fluctuations in the refractive index caused by turbulence lead to scintillation of point sources. The next generation of staring IRSTs will operate at frame rates high enough to be able to exploit these effects. The understanding of scintillation has been the subject of several international research projects which will be discussed briefly in Section 2.2.

The aim of this work is limited to obtaining a general understanding of the effects of scintillation in typical conditions to allow development of appropriate detection algorithms and representations of synthetic targets in image sequences. Accurate parameterisation of scintillation and the determination of the relationship of the parameters to meteorological conditions could be the subject of future investigations.

Target detection involves some form of spatial and/or temporal image filtering to enhance the response to targets and reduce the effect of clutter. Usually a thresholding operation is performed to isolate the brightest pixels as possible targets. These possible target locations are then passed to a tracker which establishes target tracks and can

reject tracks showing non-targetlike behaviour. In order to develop and test detection and tracking algorithms for IRST systems it is necessary to have representative image sequences of the target of interest in the range of backgrounds encountered in service. The collection of real image sequences for all the situations required would be a considerable task. A practical alternative is to generate synthetic image sequences based on mathematical models of the target and background. Synthetic targets could be placed in images of real backgrounds, or realistic backgrounds could be generated using modelling tools.

It is important that a model should as accurately as possible represent all the features of the real situation. Otherwise algorithms may be devised which perform well during development but fail in operational conditions because they were optimised on non-realistic features. Synthetic targets could be placed in images of real backgrounds, or realistic backgrounds could be generated using modelling tools such as IRTOOL (Arete Associates, Sherman Oaks, CA, USA). The insertion of synthetic targets is a more complex problem. As well as atmospheric absorption of the target emissions and radiance along the target line of sight, atmospheric turbulence and sensor effects must be modelled. Unfortunately the effect of scintillation due to atmospheric turbulence is not sufficiently understood to allow accurate target modelling from first principles. The current understanding of scintillation is discussed in Sections 2.1 and 2.2.

An alternative approach to first principle calculations is to use a phenomenological model where parameters describing the scintillation are extracted and their temporal behaviour is determined. The intrinsic parameters are the magnitude of radiance, blurring effects and image motion, and the correlation times and fluctuations in these quantities. A phenomenological model will be considered in more detail in Section 2.3.

There are additional effects that must be considered when imaging point sources. While the geometrical projection of a target at the horizon on the focal plane array (FPA) of an IRST is only a small fraction of the area of a pixel, the actual energy from the target is spread over several pixels by the blurring effect of the optics and atmosphere. In order to model the response of an IRST sensor, it is necessary to know the point spread function (PSF) of the atmosphere and the optics. It is an advantage to measure the atmospheric PSF with a system optically similar to an IRST sensor so that effects which are not fully corrected will tend to cancel between the measuring sensor and the system sensor. In this work an Amber Galileo 3-5 $\mu$ m IR camera fitted with a 300 mm lens was used as the sensor. This sensor would have similar optical properties and a similar FPA to proposed staring IRST sensors, and therefore many of the factors affecting sensor response would be related.

A further complication is that the FPA of a staring IRST consists of finite sized pixels. This means that the response of the sensor would depend on the relative location of the source image on the FPA and any small motion of the image would cause a variation of response. The effect of finite pixel size is discussed in Section 5.2. The atmospheric turbulence causes the apparent location of the source to move in a random fashion.

Furthermore, the motion of the camera would also cause apparent scintillation. Measurements of the effect of scintillation need to be made with a sensor which can quantify both image intensity fluctuations and image motion.

To obtain data for the model, measurements of the effect of atmospheric turbulence on the transmission of 3-5  $\mu\text{m}$  IR over a path of approximately 20 km over water on one day have been made. The data were analysed to give estimates of the radiance of the source image, magnitude of the scintillation fluctuations, image motion and atmospheric PSF.

The paper will consider first the standard theory of scintillation in Section 2.1 and some previous measurements in Section 2.2. A phenomenological model is proposed in Section 2.3, and the measurements of IR transmission made to obtain values for the parameters of the theory are described in Sections 3 and 4. Preliminary analysis of the raw data is presented in Section 4, and detailed analysis of the data to extract model parameters is reported in Section 5. Some conclusions on the effects of scintillation for the design of staring IRSTs are presented.

## 2. Scintillation

### 2.1 Standard theory

Radiation propagating in vacuum travels in straight lines, and if the source emits a constant flux then a sensor would give a constant response. For propagation through the atmosphere the path would be bent when passing through refractive index gradients. This means that radiation initially diverging from the line of sight between a source and sensor may be bent back toward the sensor, undergoing optical interference and hence varying the response of the sensor. Conversely radiation initially along the line of sight may be bent away from the sensor. Hence the response of the sensor can fluctuate randomly depending on the random distribution of turbulent refractive index variations between the source and sensor.

The signal fluctuations caused by scintillation follow a statistical distribution, and the distribution for small and moderate scintillation can be derived by methods described in [1, 2]. These are summarised below. Let the electric field at the sensor due to the source without scintillation be given by

$$\Phi(\underline{r}, t) = [E(\underline{r})]^{\frac{1}{2}} \exp(i \underline{k} \cdot \underline{r} - i \omega t),$$

where  $k = 2\pi/\lambda$ ,  $E(\underline{r})$  is the irradiance in  $\text{Wm}^{-2}$  in SI units,  $\Phi(\underline{r}, t)$  is the electric field in  $\text{Wm}^{-1}$ ,  $\lambda$  the wavelength and  $\omega$  the frequency and  $\underline{r}$  is position in space. In turbulence the electric field is given by

$$\Phi(\underline{r}, t) = \langle E(\underline{r}) \rangle^{\frac{1}{2}} \exp(i \underline{k} \cdot \underline{r} - i \omega \cdot t + \chi(\underline{r}, t) + i \varphi(\underline{r}, t)),$$

where  $\langle E(\underline{r}) \rangle$  is the non-fluctuation part of the irradiance,  $\chi(\underline{r}, t)$  is the fluctuating part of the magnitude, and  $\varphi(\underline{r}, t)$  is the phase angle variation.

Hence, the magnitude of the fluctuating part of the irradiance is given by

$$E(\underline{r}, t) = \langle E(\underline{r}) \rangle \exp(2\chi(\underline{r}, t))$$

In the Rytov approximation  $\chi(\underline{r}, t)$  is the weighted sum of the contributions of all the fluctuations between the camera and source, and is considered to be a random variable with a Gaussian distribution. With this approximation, the ratio of the variance of the irradiance to the square of the mean irradiance is given by

$$\frac{\sigma_E^2}{\langle E \rangle^2} \equiv \frac{\langle (E - \langle E \rangle)^2 \rangle}{\langle E \rangle^2} = \exp(4\sigma_\chi^2) - 1 = \exp(\sigma_{\ln E}^2) - 1$$

where  $\sigma_\chi$  is the standard deviation of  $\chi$ ,  $\sigma_E$  is the standard deviation of the irradiance, and  $\sigma_{\ln E}$  is the standard deviation of the natural logarithm of the irradiance. This can be rewritten as

$$\ln \left( 1 + \frac{\sigma_E^2}{\mu_E^2} \right) = \sigma_{\ln E}^2 = 4\sigma_\chi^2$$

The value of  $\sigma_{\ln E}$  can be calculated from the distribution of the values of the natural logarithm of the irradiance, or from the ratio of the irradiance standard deviation to mean.

Many measurements of scintillation have been made to try to verify a relation between the magnitude of scintillation and the bulk turbulence properties of the refractive index of the atmosphere. The spatial variation of the refractive index of the atmosphere can be described by the refractive index structure constant,  $C_n^2$  defined by

$$\langle [n(\underline{x} + \underline{r}) - n(\underline{x})]^2 \rangle = C_n^2 r^{\frac{2}{3}}$$

where  $n$  is the refractive index of the atmosphere,  $\underline{x} + \underline{r}$  and  $\underline{x}$  are two points in space,  $r$  is the magnitude of  $\underline{r}$ , and  $\langle \rangle$  denotes time average.

For a point source and point sensor the theory gives a relation between the magnitude of scintillation and turbulence over a horizontal path with constant  $C_n^2$  as  $\sigma_E^2/\mu_E^2 \approx 0.496 C_n^2 k^{1/6} L^{1/6}$ , where  $L$  is the source-sensor distance and  $\mu_E^2$  is the square of the mean of the irradiance. If the sensor has a finite size, the incident energy would be averaged over the aperture of the sensor. The effect of aperture averaging is given by the factor  $A$ , defined as the ratio of  $\sigma_E^2/\mu_E^2$  from a sensor with aperture diameter  $D$  to a sensor with an infinitesimally small aperture. Churnside [3] discusses the effect of aperture averaging under a range of circumstances, and for the case of weak turbulence studied in this work, he gives an approximate formula for  $A$

$$A = \left[ 1 + 1.07 \left( \frac{kD^2}{4L} \right)^{1/6} \right]^{-1}.$$

For values of  $L = 20000$  m,  $D = 0.124$  m and  $\lambda = 4 \times 10^{-6}$  m, the value of  $A = 0.79$ . This means that the observed ratio  $\sigma_E/\mu_E$  is reduced by a factor 0.89 by the finite aperture of the sensor optics.

The standard theory of the interaction of meteorology and scintillation identifies the main factors as the air-sea temperature difference (ASTD) and the wind velocity perpendicular to the line of sight [1]. Qualitatively, a negative ASTD due to warm sea and cool air causes unstable conditions with convection currents in regions with different refractive indices, so the greater the negative ASTD the greater the expected magnitude of scintillation. Stable conditions apply when the ASTD is positive. The temporal variation of scintillation is assumed to be due to the wind blowing the regions of variable refractive index across the line of sight.

## 2.2 Previous Measurements

There have been a number of international programs to measure IR transmission and scintillation over water.

The Low-Altitude Point-Target Experiment (LAPTEX) was conducted in Northern Summer 1996 in Crete. A description of some of the experiments was given by de Jong [4]. A number of sources were mounted on a small ship which repeatedly travelled on a path towards and away the sensor positions while measurements of transmission and scintillation were made. A range of visible and IR sensors were used, including IR cameras and a transmissometer. For one series of scintillation measurements, the source consisted of 18 tungsten lamps, each rated at 50 W, and the sensor was a Cincinnati IRC IR camera with 160x120 pixels and sensitive in the 3.7-4.6  $\mu$ m band. It was characterised by an instantaneous field of view (IFOV) of 0.1 mrad and was operated at 50 fps. de Jong [4] reports standard deviation to mean ratios as a function of range varied between 0.1 at 3 km to approximately 1.0 at 30 km on one day, and less on other days. The near IR transmissometer was characterised by a source of

wavelength  $0.85 \mu\text{m}$  and an intensity of  $750 \text{ W/sr}$  modulated at  $1000 \text{ Hz}$ . The sensor IFOV was  $5 \text{ mrad}$ . The main results were that the standard deviation to mean ratio varied from  $0.04$  at  $8 \text{ km}$  to  $0.3$  at  $26 \text{ km}$  and scintillation spectra showed correlations up to  $250 \text{ Hz}$ . There was not good correlation between the magnitude of the scintillation and the value of  $C_n^2$  derived from meteorological measurements.

The Electro-Optical Propagation Assessment in a Coastal Environment (EOPACE) was held in 1996, 1997 and 1998 over a  $15 \text{ km}$  path in San Diego Bay, USA and over a  $22 \text{ km}$  path at Monterey Bay, USA. Zeisse et al [2] described some of the instrumentation used, and Fredrickson et al [5] discussed the scintillation results. Bulk estimates of  $C_n^2$  were obtained using a buoy moored at the mid-point of the path. It was found that under unstable conditions there was good agreement between scintillation and  $C_n^2$  measurements, but the agreement was poor for neutral and stable conditions. de Jong et al [6, 7] reported similar results and conclusions as for the LAPTEX trials.

Measurements were made in the North Sea in 1994 by Schwering and Kunz [8], and Kunz et al [9]. A point source was placed on a platform at sea at heights of  $1.5 \text{ m}$  and  $7 \text{ m}$ . The sensor was placed on a pier  $19 \text{ km}$  distant at heights of  $15 \text{ m}$  and  $40 \text{ m}$ . The sensor was a  $64 \times 64$  pixel Cincinnati IRC-64A camera operating in the  $3-5 \mu\text{m}$  band at  $25 \text{ Hz}$ . The lens had an aperture of  $30 \text{ cm}$  and a focal length of  $1 \text{ m}$ , giving an IFOV of  $0.028 \text{ mrad}$  on pixels with  $0.05 \text{ mrad}$  spacing (30% fill factor). Schwering and Kunz developed a theoretical model and compared it with their measurements of contrast, skewness, ellipticity, kurtosis and diameter. They reproduced limited data which showed considerable scatter in the relation between image size and contrast. The agreement with the model was not good. Kunz et al used a measure of size or blur a distance derived from a transversal coherence length, which varied between  $1.5$  to  $2.5$  pixels. They reproduced scatter diagrams between calculated and measured parameters which showed mainly weak correlations. There were no measurements of image motion or of the effect of the finite pixel size on the performance of the FPA sensors.

The main conclusion of the trials was that reasonable agreement between theory and measurement could be obtained for unstable ASTDs, but agreement was poor for stable and near neutral conditions.

Kolnle et al [10] made measurements of point targets at long ranges with a GEC DUWIR camera equipped with a  $2^\circ$  field of view telescope giving an IFOV of  $0.08 \text{ mrad}$ . Both  $3-5 \mu\text{m}$  and  $8-12 \mu\text{m}$  bands were used, and the frame rate was  $25 \text{ frames/s}$ . A plot of signal to noise ratio for a sequence of  $750$  frames for a point target moving between ranges of  $18.5$  to  $26.5 \text{ km}$  was given. The presence of fluctuations due to scintillation was noted.

### 2.3 Phenomenological model

The generation of realistic synthetic image sequences of a point target at long range low over water requires a method of calculating the effect of scintillation. The experimental results to date indicate that it is not possible to start from meteorological variables and calculate scintillation from first principles. An alternative is to use a phenomenological model of scintillation based on a few parameters which are fitted to measurements of scintillation made under controlled conditions. A series of measurements of scintillation could be made over a range of meteorological conditions and the data analysed to give the probability distribution functions of parameters describing the scintillation.

Kolnle et al [10] proposed a sensor model of an IRST for use in predicting detection ranges. The model included a range of parameters defining the sensor, targets and background. Scintillation was described by signal fluctuation and the ratio of blur size to pixel size, but details were not given and so this model is not able to be used to generate target images.

The aim of the current work is to propose a phenomenological model of the effect of scintillation which is sufficiently detailed and accurate to be used to generate realistic synthetic targets. The general idea is that atmospheric turbulence causes fluctuations in brightness, apparent size and location of the point source. It is necessary to quantify the magnitude and temporal behaviour of these fluctuations.

The characteristic of the image of a point source after transmission through the atmosphere and optics is the point spread function (PSF) due to the effects of the atmosphere and sensor. The PSF will be modelled by a 2D Gaussian given by

$$PSF = A \cdot \exp \left( -\frac{(r - r_0)^2}{2\sigma_r^2} - \frac{(c - c_0)^2}{2\sigma_c^2} \right)$$

The parameters defining the PSF are  $A$  = maximum,  $r$  = row direction coordinate,  $c$  = column direction coordinate,  $r_0$  = the row direction coordinate of the maximum,  $c_0$  = column direction coordinate of the maximum,  $\sigma_r$  = standard deviation of row direction location and  $\sigma_c$  = standard deviation of column direction location. It will be assumed that the PSFs are circularly symmetric. The assumed form of the PSF means that vertical sections through the maximum of the PSF are Gaussians.

The values of the parameters in an image sequence are the result of the sum many random fluctuations, and so in the absence of other influences, their probability distributions will tend to form Gaussian distributions. However there may be correlations between different parameters and temporal correlations between the values of the same parameters on sequential frames. The degree of correlation would have to be determined from experimental measurements. The temporal development

of the parameters of scintillation will be modelled as first order Markov sequences quantified by a single correlation time each, which would be determined experimentally.

In particular, the data required to model scintillation are:

- Mean and standard deviation of the magnitude of the PSF.
- Mean and standard deviation of the width of the PSF.
- Standard deviations of the row and column direction PSF locations.
- Temporal correlation coefficients of the above parameters.
- Coefficients of any correlations between the above parameters.

Measurements of the probability distributions of these parameters for a particular set of meteorological conditions will be made in this work.

In a practical application, a target image sequence would be constructed frame by frame, possibly in real time, by calculating the values of the parameters from the general conditional probability distribution [11]

$$p_2(y_1|y_2, \tau) = \frac{1}{\sqrt{2\pi(1-\exp(-2\tau/\tau_r))\sigma_y^2}} \exp\left\{-\frac{[(y_2 - \mu_y) - \exp(-\tau/\tau_r)(y_1 - \mu_y)]^2}{2(1-\exp(-2\tau/\tau_r))\sigma_y^2}\right\},$$

where  $y_1$  is the new value of the parameter,  $y_2$  is the value of the parameter in the previous frame,  $\tau_r$  is the correlation time,  $\tau$  the time step, and  $\sigma_y^2$  and  $\mu_y$  are the standard deviation and mean of the parameter. The unconditional probability distribution is

$$p_1(y) = \frac{1}{\sqrt{2\pi\sigma_y^2}} \exp\left\{-\frac{(y - \mu_y)^2}{2\sigma_y^2}\right\},$$

and the correlation function is

$$C_y(\tau) = \sigma_y^2 e^{\frac{-\tau}{\tau_r}}.$$

Since the maxima of the PSFs are characterised by a log Gaussian distribution, the model values of PSF maxima would be given by the exponential of the value from the conditional Gaussian distribution.

## 2.4 Effect of finite sensor size on imaging of point sources

The measurement of scintillation with a focal plane array (FPA) camera is complicated by the discrete nature of the sensing elements. There are two effects on the observed radiance; the reduction in pixel value caused by the PSF overlapping adjacent pixels which is aggravated when the source is not imaged in the centre of a pixel, and the fact that the observed radiances are the result of integration of the PSF over the sensitive areas of the individual pixels. The off-centre effect will be discussed first.

The observed radiance will be affected by the position of the image relative to the pixel centre. The PSF centre can vary up to  $\pm 0.5$  pixel spacings in the row and column directions from the centre within the pixel where it was detected, or else it would be detected in an adjacent pixel. If the size of the PSF is much smaller than the pixel, the response would be approximately constant for locations over the sensitive area of the pixel, but near zero in the dead areas between pixels. For the case where the PSF of the point source is comparable to the pixel size, when the image is off centre the response of the pixel containing the centre of the source image is reduced and the response of adjacent pixels is increased. If there is camera motion due to jitter in the mounts, or other causes, there would be apparent scintillation on top of any atmospheric scintillation. Image motion caused by the atmosphere would also add to this effect. If the PSF is much larger than the pixel the effect of image location on response would be minimal. These issues have been discussed in the literature [12-15]. Kolnle et al [10] considered the effect of finite pixel size on the response of their sensor, but they did not give any method for quantifying the effect, or of measuring the ratio of PSF size to pixel size.

A further correction is required to the measured radiance values. The experimental radiance measurements are integrals of the continuously variable true PSF over the sensitive areas of the pixels of the FPA. To obtain the true PSF a transformation is required from the measured, integrated values to the original PSF. The way to calculate this effect is not obvious. One way would be to fit a 2D PSF to the radiance values of the pixels containing the source image, but this approach is not practical for a number of reasons. The exact form of the PSF is not known, and the radiance values are very coarse and noisy, so any fit procedure is likely to be unstable. It is conceptually simpler to reverse the procedure and calculate the integrated values from a standard hypothesised PSF and then use these to calculate a correction to the original integrated values.

Methods of correcting for the finite pixel effect have been developed and are described in Appendix F.

### 3. Experimental

#### 3.1 Site location

Scintillation measurements were made over Gulf St. Vincent off the coast of suburban Adelaide. A map of the area is given in Appendix A. The camera was located in the Henley Beach Surf Club observation room at a height of approximately 30 m above sea level. The source was located on cliff tops at Lonsdale and O'Sullivans Beach at heights above sea level of approximately 30 m. The source-camera distance for Lonsdale is 17.0 km and O'Sullivans Beach 19.9 km.

#### 3.2 Source

The source was an AIRA Infrared Gas Heater from AIRA Pty Ltd, Kilsyth, Victoria, Australia. It consisted of a double element burner of total area 190x230 mm, and a nominal total output of 4 kW. A wind shield in the form of a square duct was fitted to reduce variations in output caused by wind gusts. Attenuation filters were used on the source to obtain a range of signal-to-noise (SNR) values. The filters consisted of aluminium plates with regular patterns of 2 mm diameter holes. The number of holes determined the amount of transmission. The source was not calibrated since absolute values of transmission were not required, scintillation being quantified by the ratio of the standard deviation to mean.

#### 3.3 IR sensor

IR image sequences were obtained using an Amber Galileo 3-5  $\mu\text{m}$  infrared camera with a signal resolution of 12 bits. The Galileo focal plane array is 256x256 pixels, with pixel pitch 30  $\mu\text{m}$ . The camera was fitted with a 300 mm catadioptric lens (Diversified Optical Products, Inc, Salem, N.H., USA) which gave rise to an IFOV of 0.1 mrad. The field of view (FOV) was 1.467°. The camera was set up to output images from a sub-window of 64x64 pixels. The images were recorded on a Windows NT PC using Videosavant software (IO Industries Inc. London, ON, Canada). The point spread function (PSF) of the optics was given by the manufacturer as diameter of the circle in the focal plane containing 85% of the energy of a point source. The size of the 85% blur circle varied with position on the focal plane, and the values are:-

On-axis	Off-axis
	3.61°, 3.61mm
0.0014"	0.0018"
35.6 $\mu\text{m}$	45.7 $\mu\text{m}$
	5.16°, 9.0mm
	0.0023"
	58.4 $\mu\text{m}$

### 3.4 Meteorological conditions

It was not possible to make meteorological measurements along the observation path. However, data was obtained for a number of other sites in the region. Measurements of the air temperature and the surface water temperature near the camera position off the jetty at Henley Beach were obtained at several times. Meteorological conditions were measured by the National Tidal Authority at Pt Stanvac, and at Adelaide Airport and Noarlunga by the Bureau of Meteorology. Details of meteorological conditions are given in Appendix B. Over the time of the trial the air-sea temperature difference changed from about  $-2^{\circ}\text{C}$  to  $-1.1^{\circ}\text{C}$ . The wind direction was approximately south west, and the speed increased from 1.7 m/s to 5 m/s.

### 3.5 Data file codes

Data were collected at the Lonsdale site, both in the absence of a spectral filter and with a 4.42-5.46 $\mu\text{m}$  filter. Since the camera was only sensitive to a maximum of 5  $\mu\text{m}$ , the effective filter width was 4.42-5  $\mu\text{m}$ . Data were collected from the O'Sullivan's Beach site without the spectral filter. Attenuation filters were used on the source to obtain a range of signal to noise (SNR) values. The attenuators consisted of aluminium plates with regular patterns of 2 mm diameter holes. The number of holes determined the amount of transmission. The attenuation filters were identified by the codes defined in Table 1.

*Table 1. Codes for attenuation filters*

Transmission	No camera filter	4.42-5.46 $\mu\text{m}$ filter
No attenuation	Nf	F5f
Half transmission	Nh	F5h
Quarter transmission	Nq	F5q
Eighth transmission	Ne	F5e
Sixteenth transmission	Ns	F5s
Background	Bg	Bgf5

The different data runs were identified by codes which included the time of observation, eg Nh1027 was initiated at 1027 hrs. The code for calibration runs started with the calibration temperature followed by the time, eg 251118 identified a run at  $25^{\circ}\text{C}$  at 1118 hrs. The camera was turned on 0855 hrs to allow sufficient time for equilibration.

Two point non-uniformity corrections (NUCs) were conducted at  $25^{\circ}\text{C}$  and  $55^{\circ}\text{C}$  with a large area blackbody. The inbuilt software in the camera was used for the NUC. Calibration measurements at 25, 40 and  $55^{\circ}\text{C}$  were made by flood-filling the lens with a large area black body at the nominated temperatures. The lens focus settings were the

same as those used for the data acquisition for the filtered and unfiltered cases. Details of the recording runs are given in Appendix C.

## 4. Results

### 4.1 Data analysis

Much of the data analysis was done using spreadsheets. Gaussian curve fitting was done with the CurveExpert 1.3 software (Daniel Hyams, [www.ebicom.net/dhyams/cvxpt.htm](http://www.ebicom.net/dhyams/cvxpt.htm)). Special C programs were written to calculate maximum and total signal magnitudes, target motion and location, temporal correlations and point spread functions. Image sequences were displayed using the Gabriel software (Aspect Computing, Adelaide, Australia).

### 4.2 Calibration

The non-uniformity correction (NUC) procedure built in to the camera fits a linear equation to a two-point calibration. However, the response of the camera is non-linear. To obtain a more accurate calibration, a three point calibration was conducted using the response to black body temperatures of 25, 40 and 55°C. The blackbody radiance for each temperature was calculated over the bands 3-5  $\mu\text{m}$  and 4.42-5  $\mu\text{m}$ . The image sequences at each temperature were averaged to give a reference frame at each temperature. For the same pixel location of each on the 3 temperature frames, the pixel counts and corresponding calculated radiance values were fitted with a quadratic function. The coefficients of the fit were stored in files for each calibration and were used to calibrate the raw data.

Image size and location variables were converted from pixel spacing values to absolute angular units by the factor 1 pixel = 0.1 mrad.

### 4.3 Registration and background subtraction

The background surrounding the source at both locations was very cluttered. In each case 5000 frames of background were recorded with the camera aligned with the same line of sight as for the data collection. To remove the effect of random noise, a reference background frame was obtained by averaging each pixel over the 5000 frames. Small drifts in overall radiance occurred between measuring the background, and source data, caused by solar heating of the background. To allow for these drifts, regions surrounding the source location in the data frame and background frame were averaged and the background level adjusted additively to match the data area.

After completion of data collection it was discovered that a vertical motion of unknown source with a maximum amplitude of the order of one pixel spacing sometimes occurred in a sequence. It was decided to eliminate the effect of the motion

by registering the background with the data frame by frame and then subtracting the background to obtain the source signal. The motion appeared to be only in one direction, which reduced the complexity of the registration procedure.

The following procedure was used to register the background frame to each data frame. A highly cluttered area of the background frame in the vicinity the source location was chosen for registration. The whole frame was not used in order to reduce the amount of computation, and also because large regions of low gradient would have only added noise. At each pixel location in the background a symmetrical 5 point spline in the vertical direction was fitted to the 5 pixels centred on the pixel of interest. The spline coefficients were used to interpolate between the pixel centre positions allowing images shifted by sub-pixel amounts to be calculated. The background frame was shifted from -2.5 pixel spacings to +1.5 pixel spacings in 0.05 pixel steps and the correlation with the image area on the data frame calculated. The background at the best correlation position was subtracted to give the signal from the source. The degree of correlation was calculated both by summing the multiples the background and data radiance values, and also by minimising the sum of the absolute differences. It was found that the latter method was more stable and was used for all cases.

The data after the preceding processing still showed the motion of the source due to the camera motion. This motion would have been eliminated if the data frame and not the background frame had been shifted. The data frames were not shifted into registration because the very large gradients in the region of the source showed up the inaccuracies in the spline fit, giving spurious values for the source. Shifting the background image was also more computationally efficient as the coefficients of fit had to be calculated only once. The actual apparent motion of the source in each frame was given by the difference between the measured source motion and the calculated background motion. This procedure gave approximately isotropic average source motion, so it was likely to be sufficiently accurate.

#### 4.4 Magnitude of apparent scintillation in the raw data

The magnitude of scintillation in the raw data is of interest because it is similar to the scintillation that would be seen by an IRST sensor. However, to determine the true magnitude of the scintillation, any image motion caused by the atmosphere and camera jitter, and also the pixel size effect must be accounted for. Initially the data will be analysed to determine apparent scintillation in the raw data, and in Section 5.2 the effect of image motion and the point spread function will be determined.

The maximum value of the source in each frame was recorded, and the radiance values in the 3x3 pixel square centred on the maximum value were summed to give the total signal from the source. A plot of maximum measured source radiance in each frame vs frame number for sequence nf1025 is shown in Figure 1. It can be seen that the distribution is asymmetrical with greater deviations in the higher magnitude direction. The Rytov theory of scintillation predicts that the signal magnitude distribution is

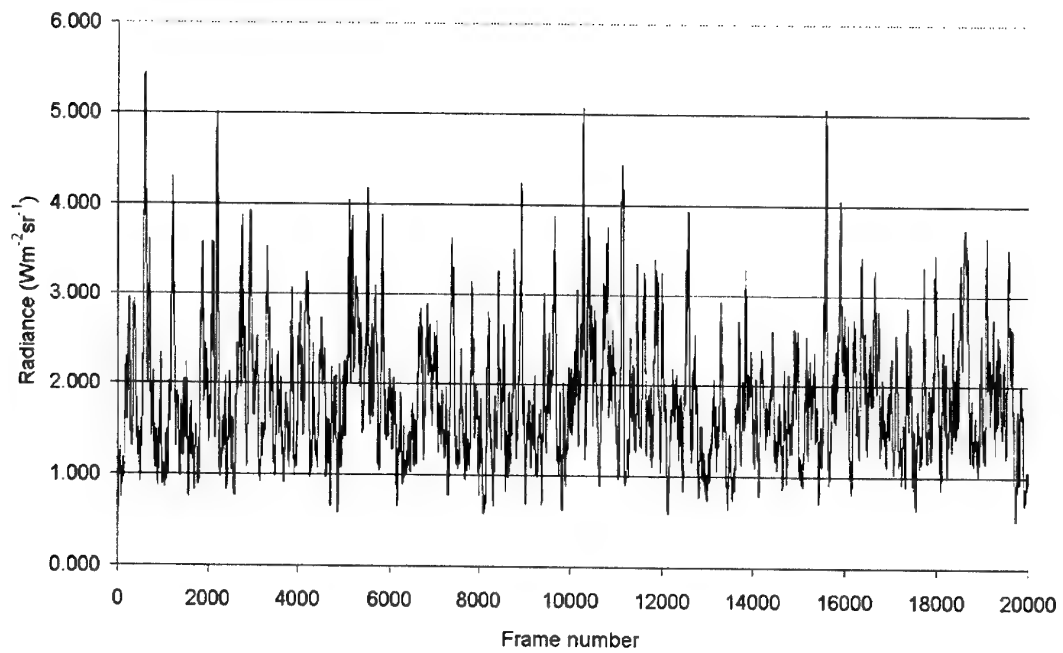


Figure 1. Measured source radiance vs frame number for sequence nf1025

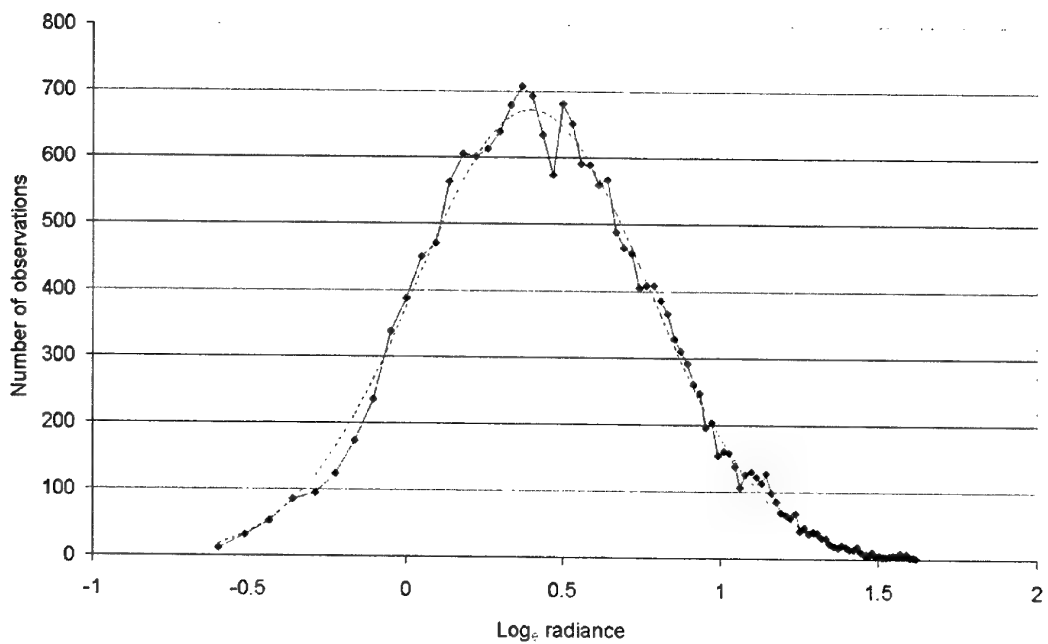


Figure 2. Histogram of log radiance values from sequence nf1025. Solid curve observed values, dotted curve fitted Gaussian

log-Gaussian. A histogram of the natural logarithms of the observed radiance values is plotted in Figure 2, together with a fitted Gaussian curve. It can be seen that the observations are well fitted by a Gaussian.

Histograms were made of log signal magnitudes for all image sequences and the resulting curves were fitted by Gaussians. The correlation coefficients were nearly always greater than 0.98, indicating that the distributions were close to Gaussians. The values of the mean and the standard deviation of the log distribution of the signal maximum and total from the Lonsdale site with no filter are given in Appendix D. Theory indicates that there is a relationship between the standard deviation calculated from the log-Gaussian distribution and from the ratio of the standard deviation to mean of the measured radiance magnitude distribution. The overall values of the ratios of standard deviations to means calculated from both the Gaussian fits and the raw radiance distributions are summarised in Table 2. The values were estimated from an amalgam of the attenuated and unattenuated values taking into account the correlation coefficients and likely accuracy. The agreement is quite good, with the direct values being about 10% less than the Gaussian values.

*Table 2. Ratio of standard deviation to mean of radiance distributions calculated from Gaussian fit and directly.*

	Standard deviation/mean	
	Gaussian	Direct
Lonsdale no filter, maximum	0.41	0.38
Lonsdale no filter, total	0.37	0.36
Lonsdale filter, maximum	0.49	0.47
Lonsdale filter, total	0.39	0.36
O'Sullivan's Beach, maximum	0.67	0.59
O'Sullivan's Beach, total	0.62	0.57

#### 4.5 Temporal correlation of observed signal magnitudes

The temporal correlation of the image maxima was calculated from the correlation coefficient between the sequence and the same sequence shifted by progressively increasing number of frames. The correlation time was taken to be the time for the correlation to fall to a value of  $1/e$ . To test the variability during a run, the 20000 frames of the sequence were broken up into 5 lots of 4000 frames. The means of the 5 lots and standard deviations between the lots are given in Appendix E and the overall means are given in Table 3. There was some scatter between lots, but it was not significant. The correlation time varied between 0.027 s and 0.147 s. The very low values for the filtered data may be due to the lower radiance values from the source, which would increase the randomising effect of noise.

Table 3. Correlation times of radiance fluctuations

Lonsdale	Correlation time (frames)					Overall	Correlation time (s)
	nf1025	nh1027	nq1029	ne1031	ns1033		
Maximum Mean	37.6	53.6	45	43.6	37.4	43.4	0.146
Total Mean	38.8	51.4	50.4	43	35	43.7	0.147
Lonsdale filter	f5f1222	f5h1225	f5q1227	-	-	-	-
Maximum Mean	7.2	7	6.8	-	-	7	0.028
Total Mean	7	6.6	6.4	-	-	6.7	0.027
O'Sullivan's Beach	nf1508	nh1510	nq1512	ne1514	ns1516	-	-
Maximum Mean	17.8	15.4	16.8	19.3	17.2	17.3	0.058
Total Mean	19.4	15.2	17.8	20	19.4	18.4	0.062

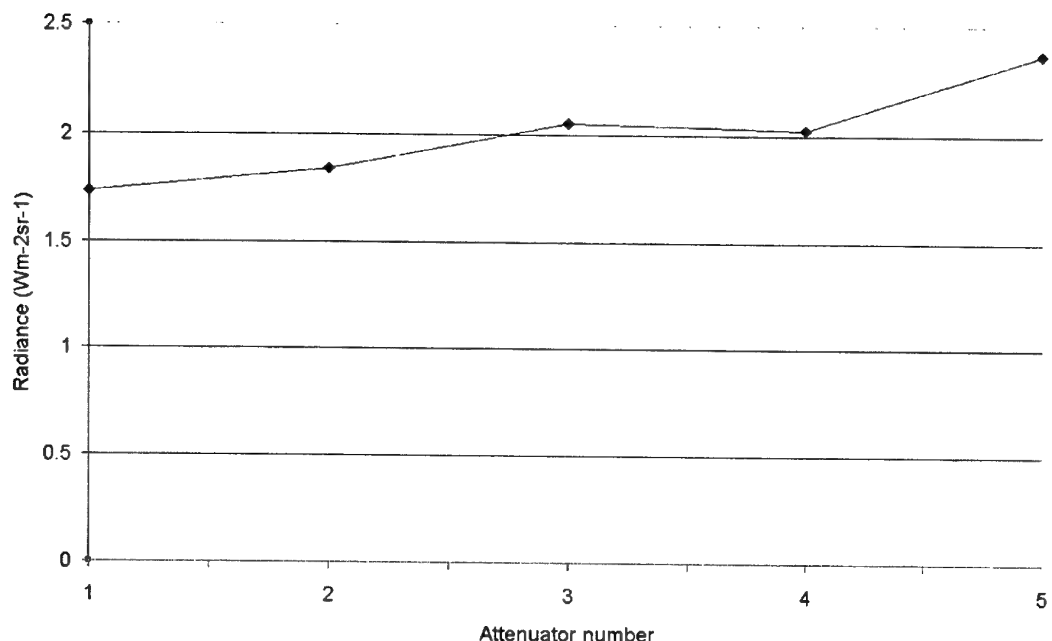


Figure 3. Predicted and observed mean of log Gaussian distribution of radiance for Lonsdale, no filter. Solid line observations, dotted line prediction.

#### 4.6 Effect of attenuators

The derivation of the log-Gaussian relationship between the signal magnitude and the magnitude of the scintillation fluctuations involved a number of approximations. As a check on the linearity of the relation with signal strength, the values of radiance corresponding to the mean of the log-Gaussian distribution of signal maxima from Lonsdale (no spectral filter) are plotted in Figure 3 against the run number. The radiance values have been multiplied by the inverse of the attenuation factor. It can be seen that while the values were approximately constant, there was a small increase

with increasing attenuation. It is not clear if this represents a slight non-linearity, or is caused by errors due to the decreasing signal-to-noise ratio. Similar behaviour was seen with the other image sequences. The values of the standard deviation were close to constant over the range of attenuations.

## 5. Discussion

### 5.1 Corrected radiance maxima and point spread functions

The data in the Results section are particular to the Amber Galileo camera. In order to determine the intrinsic effects of the atmosphere, the data must be further processed to extract the properties of the PSF which are independent of the particular sensor. The combined PSF of the atmosphere and optics as measured by the Galileo camera will be calculated first. This process will give estimates of the maximum and width of the PSF, and the row and column coordinates of the maximum. An approximate correction for the effect of the finite pixel size of the FPA will be used to calculate estimates of the sensor independent PSF maximum and width. The atmospheric and optics components of the PSF will then be calculated. The distribution of the instantaneous locations of the PSF maxima will be calculated, and then the correlation times of the PSF motions. These are all parameters that are required for the phenomenological model.

The PSF due to the combined effects of the atmosphere and optics was estimated by fitting a 1D Gaussian function to the image area centred on the pixel with maximum radiance. The exact shape of the PSF was not known, but it was expected that a Gaussian would be a good approximation. A further advantage of using Gaussians is that many calculations are mathematically tractable. If the centre of the source was imaged in the exact centre of a pixel, a Gaussian could be fitted relatively easily. In the general case the image of the source was not centred in a pixel, so a more complex procedure was necessary. A truncated peak climbing method was used as illustrated in Figure 4. A Gaussian function was fitted to 3 pixels in a column centred on the maximum pixel, and also to the 2 corresponding adjacent columns. The position of the centre of the source had to be located between the 2 highest Gaussian maxima. This point was estimated by fitting a Gaussian to the line containing the two maxima, and the point on the third column on the intersection of the column and a line joining the two maxima. The radiance value at this point on the column was obtained from the fitted Gaussian. The maximum of the Gaussian fitted to these 3 points was taken to be the corrected value of the maximum of radiance. Because of noise and some low radiance values, this procedure resulted in a few values which were unrealistic and these were rejected, but for the unattenuated cases the rejections were only a few percent of the total. The parameters of the combined PSF were estimated from the calculated maximum value and subpixel location and are given in Table 4. Sequence f5h1225 suffered excessive camera motion which prevented the calculation of accurate values. The calculated PSF widths were very similar, although there was more scatter

in their standard deviations. The attenuated data sets gave more scattered values because the signal to noise levels were lower.

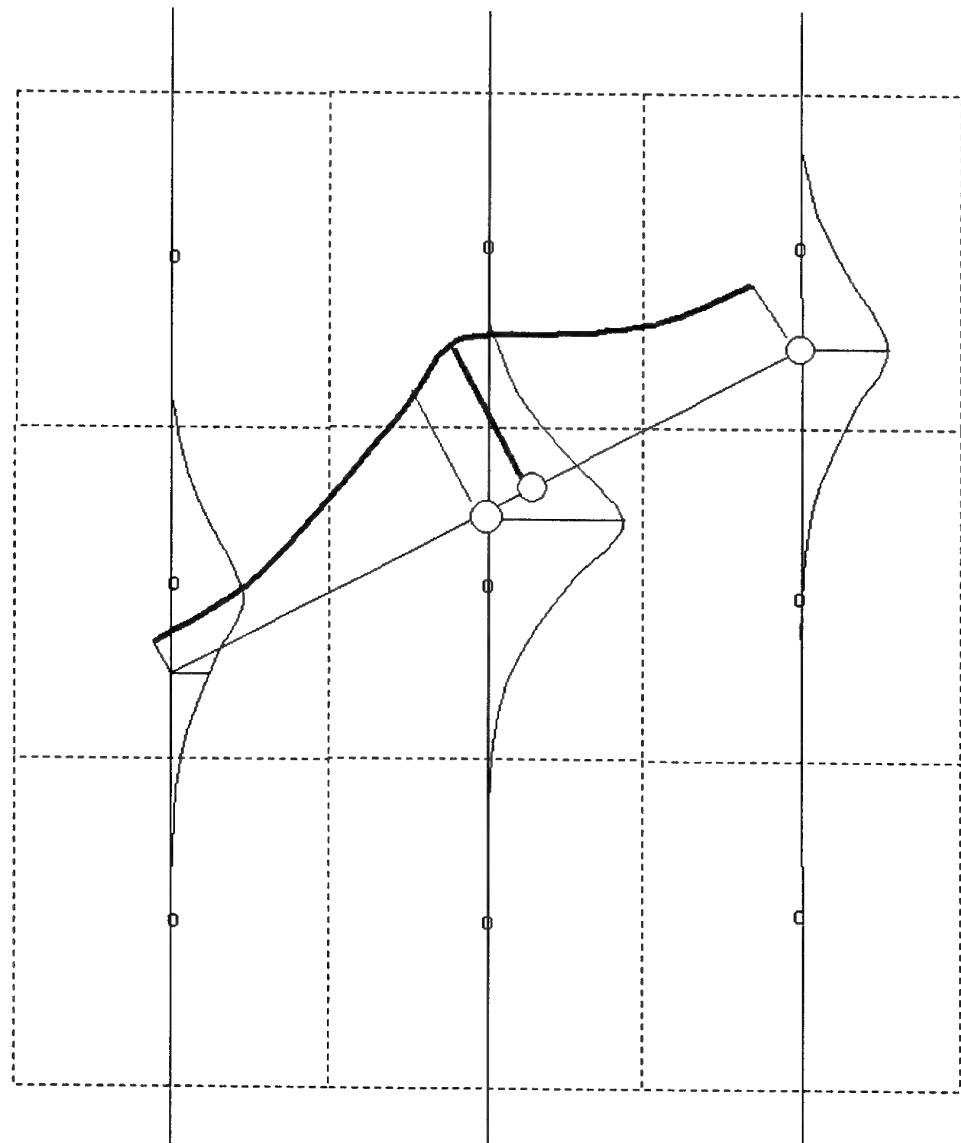


*Fig 4. Representation of the method fitting a Gaussian distribution to observed pixel values.*

Table 4. Calculated width of the point spread functions at the 2 locations.

Lonsdale	nf1025	nh1027	nq1029	ne1031	ns1033
PSF width (Pixels)	0.64	0.63	0.65	0.72	0.72
Standard deviation of width (Pixels)	0.054	0.058	0.099	0.21	0.25
Lonsdale with filter	f5f1222	F5h1225	f5q1227		
PSF width (Pixels)	0.64		0.59		
Standard deviation of width (Pixels)	0.123		0.26		
O'Sullivan's Beach	nf1508	nh1510	nq1512	ne1514	
PSF width (Pixels)	0.64	0.65	0.71	0.76	
Standard deviation of width (Pixels)	0.078	0.106	0.16	0.30	

## 5.2 Effect of finite pixel size

The measurement of scintillation with a focal plane array (FPA) camera is complicated by the discrete nature of the sensing elements. There are two effects on the observed radiance; the reduction in pixel value caused by the PSF overlapping adjacent pixels which is exacerbated when the source is not imaged in the centre of a pixel, and the fact that the observed radiances are the result of integration of the PSF over the sensitive areas of the individual pixels. The off-centre effect will be discussed first.

In the case of the Galileo camera the pixel spacing is 30  $\mu\text{m}$  on side and the sensitive area is 27  $\mu\text{m}$  on side, giving a fill factor of 80 %. The 85% energy spot diameter of the optics is 35.6  $\mu\text{m}$ , which is of the same order as the pixel size. If the image of a point is centred on the pixel then most of the energy should fall on that pixel, and little on adjacent pixels. The fact that the PSF is comparable in size to the pixel can be used to simplify the analysis to obtain estimates of scintillation parameters.

The observed radiance will be affected by the position of the image relative to the pixel centre. The PSF centre can vary up to  $\pm 0.5$  pixel spacings in the row and column directions from the centre within the pixel where it was detected, or else it would have been detected in an adjacent pixel. If the size of the image is much smaller than the pixel, the response would be approximately constant for locations over the sensitive area of the pixel, but near zero in the dead areas between pixels. For the case where the PSF of the point source is comparable to the pixel size, when the image is off centre the response of the pixel containing the centre of the source image would be reduced and the response of adjacent pixels increased. If there was camera motion due to jitter in the mounts, or other causes, there would be apparent scintillation on top of any atmospheric scintillation. Image motion caused by the atmosphere would also add to this effect. If the PSF is much larger than the pixel the effect of image location on response would be minimal.

A further correction is required to the measured radiance values. The experimental radiance measurements are integrals of the continuously variable true PSF over the

sensitive areas of the pixels of the FPA. To obtain the true PSF a transformation is required from the measured, integrated values to the original PSF. Both the magnitude and width, given by the standard deviation, are affected. The way to calculate this effect is not obvious. One way would be to fit a 2D PSF to the radiance values of the pixels containing the source image, but this approach is not practical for a number of reasons. The exact form of the PSF is not known, and the radiance values are very coarse and noisy, so any fit procedure is likely to be unstable. It is conceptually simpler to reverse the procedure and calculate the integrated values from a standard hypothesised PSF and then use these to calculate a correction to the original integrated values. Details of the correction procedure are given in Appendix F.

Table 5. Correction factors for the integration effect on PSF.

Shift from centre	0	0.1	0.2	0.3	0.4	0.5
Standard deviation =0.5						
Factor for maximum	1.339	1.336	1.328	1.315	1.299	1.286
Factor for standard deviation	0.855	0.856	0.859	0.864	0.870	0.875
Standard deviation =0.6						
Factor for maximum	1.235	1.235	1.232	1.227	1.222	1.220
Factor for standard deviation	0.895	0.895	0.896	0.898	0.900	0.901
Standard deviation =0.7						
Factor for maximum	1.172	1.172	1.172	1.169	1.169	1.167
Factor for standard deviation	0.921	0.921	0.921	0.922	0.922	0.923
Standard deviation =0.8						
Factor for maximum	1.132	1.132	1.132	1.132	1.130	1.130
Factor for standard deviation	0.938	0.938	0.938	0.938	0.939	0.939

The values of the correction were found to be dependent on the standard deviation of the uncorrected PSF, but only slightly dependent of the distance from the pixel centre. A summary of the correction factors to the height and width of the PSFs as functions of raw PSF width and displacement of the PSF from the pixel centre are given in Table 5.

### 5.3 Point spread functions of the optics and atmosphere

The combined blurring effect of the optics and the atmosphere is quantified by the measured PSFs. The PSF of the atmosphere alone could be obtained by a 2D deconvolution of the measured total PSF and the optics PSF. Detailed knowledge of the functional form of the PSFs would be required as well as the spatial function of the sensitive area of the FPA pixels. This procedure would be necessary if subtle differences in atmospheric effects, or other parameters, were being studied. In the present work it is only intended to obtain indicative estimates of the scintillation effects, and some approximate methods will be used.

For computational tractability, the PSFs have been approximated by assuming that plane sections through them can be given by Gaussians. Because the PSFs are

approximated by Gaussian functions, the variance of the combined PSF is given by the sum of the variances of the individual PSFs. Conversely, the variance of the atmospheric PSF can be obtained as the difference between the combined variance and the optics variance. Details of the calculations of the atmospheric and optics PSFs are given in Appendix G, and the resulting standard deviations of the PSFs are summarised in Table 6.

*Table 6. Calculated standard deviations of PSFs.*

	Observed (Pixels)	Observed (mrad)	Optics (mrad)	Atmosphere (Pixels))	Atmosphere (mrad)
Lonsdale no filter	0.58	0.058	0.031	0.49	0.049
Lonsdale filter	0.56	0.056	0.031	0.46	0.046
O'Sullivan's Beach	0.59	0.059	0.031	0.50	0.050

#### 5.4 Temporal correlation of PSF width

The temporal correlation of the width of the PSF was calculated in a similar manner to the radiance correlation. The values given in Table 7 are about half those for the maximum radiance correlation times but follow the same trend. The value for nh1027 appears to be anomalous, and an unrealistically short time was calculated for the Lonsdale filter case, possibly because of the low radiance values from the filtered sequences.

*Table 7. Correlation times for PSF widths.*

Lonsdale no filter	nf1025	nh1027	nq1029
Correlation time (s)	0.074	0.182	0.050
O'Sullivan's Beach	nf1508	nh1510	nq1512
Correlation time (s)	0.024	0.020	0.014

#### 5.5 Image motion due to scintillation

The positions of the maximum values of radiance, in row and column pixel coordinates, were derived as part of the PSF calculation. The standard deviations from the fitted histograms of the corrected row and column coordinates of the PSF maxima quantify the motion of the image of the source. The standard deviation values are given in Tables 8-10. It can be seen that the standard deviations for the row location of the unfiltered cases are approximately 0.1 pixel spacings and up to twice this for column values. It may be that there was some horizontal camera motion which broadened the column distributions. The values for the Lonsdale filter sequences were about 0.15 pixel spacings.

*Table 8. Location and motion parameters for Lonsdale, no filter.*

	nf1025	nh1027	nq1029	ne1031	ns1033
Row Standard deviation (Pixels)	0.11	0.096	0.091	0.12	0.12
Correlation coefficient	0.993	0.995	0.997	0.996	0.998
Column standard deviation (Pixels)	0.15	0.11	0.091	0.19	0.13
Correlation coefficient (Pixels)	0.985	0.981	0.997	0.958	0.991

*Table 9. Location and motion parameters for Lonsdale with filter.*

	f5f1222	f5h1225	f5q1227
Row Standard deviation (Pixels)	0.18	0.12	0.22
Correlation coefficient	0.998	0.996	0.988
Column standard deviation (Pixels)	0.14	0.19	0.16
Correlation coefficient (Pixels)	0.961	0.958	0.928

*Table 10. Location and motion parameters for O'Sullivan's Beach.*

	nf1508	nh1510	nq1512	ne1514
Row Standard deviation (Pixels)	0.093	0.090	0.11	0.10
Correlation coefficient	0.998	0.999	0.999	0.996
Column standard deviation (Pixels)	0.19	0.15	0.18	0.19
Correlation coefficient (Pixels)	0.964	0.983	0.984	0.964

## 5.6 Temporal correlation of image location

The temporal correlation of the row and column coordinates from the PSF was calculated in a similar manner to the radiance correlation. The correlation time was defined as the time required for the correlation to fall to  $1/e$ . The consistency of the data varied in the different cases. An example of consistent data from nf1508 is given in Figures 4 and 5. It can be seen that the row position does not vary significantly over long times but the column data does show a variation over a few hundred frames. The row data was corrected for camera motion but the column data was not. It is not certain that there was not some camera motion in the column direction and that this motion was superimposed in the atmospheric disturbance causing the greater variation. The longer time variation in the column data is reflected in the correlation plots shown in Figure 5.

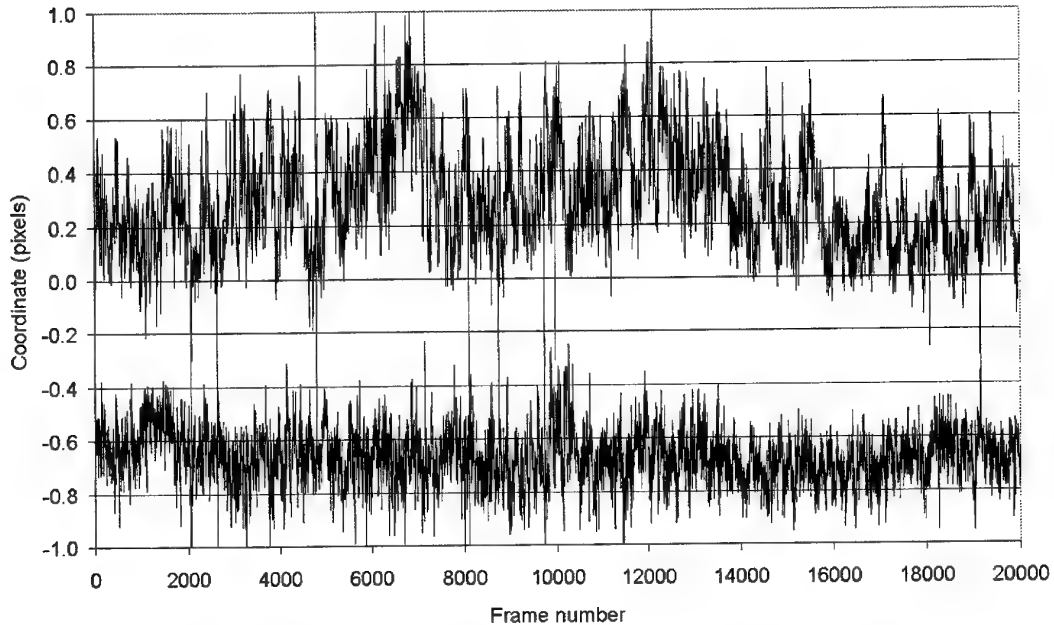


Figure 5. Coordinates from case nf1508 vs frame number. Column coordinate top curve and row coordinate bottom curve.

Tables 11 to 13 give the correlation times in terms of the number of frames and the times in seconds. The filtered Lonsdale data were very scattered because the low values of radiance decreased the accuracy of the PSF calculations and made the location values unreliable. The results for the unfiltered row cases were more consistent, the column data being more scattered. These results confirm the observations from Figures 5 and 6.

These values are of the same order and show the same trend as the correlation times for the PSF maxima from Table 3, with the times at O'Sullivan's Beach being shorter.

### 5.7 Correlations between parameters

Any accurate phenomenological model must include any correlations between parameters. To determine the extent of correlation between PSF maximum and width, maximum and location, width and location, and row and column locations scatter diagrams were made of the relevant parameters. Representative plots are shown in Appendix H. There was no obvious correlation between the parameters and it can be assumed that all parameters were independent.

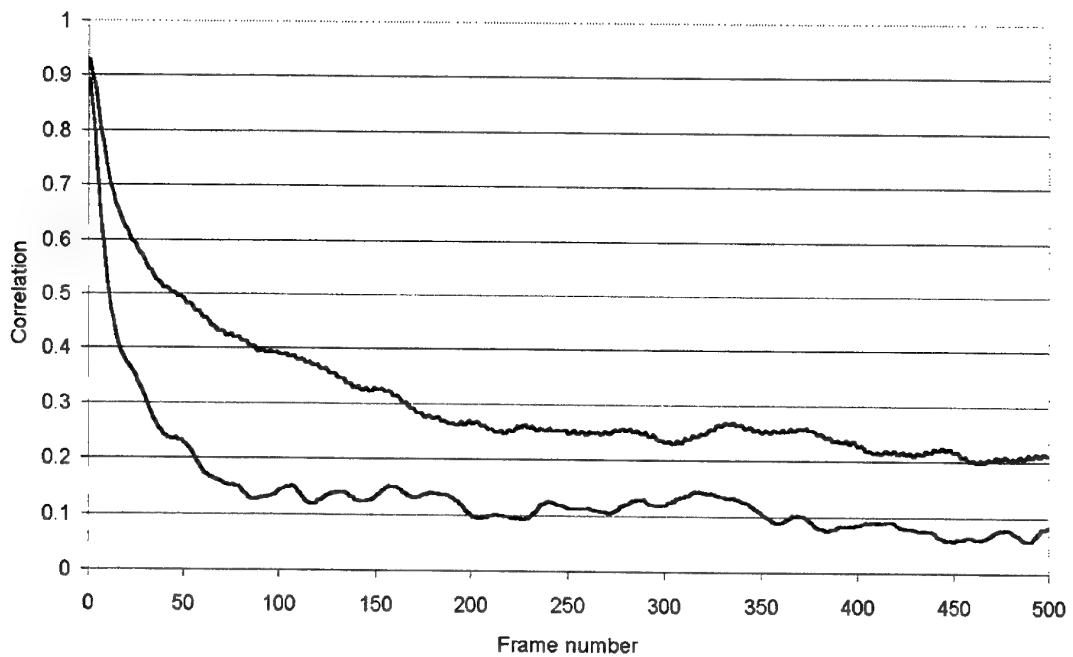


Figure 6. Coordinate correlation vs frame difference for nf1508. Column coordinate top curve and row coordinate bottom curve.

Table 11. Correlation times for location variables for Lonsdale, no filter.

	nf1025	nh1027	nq1029	ne1031	ns1033
Row					
Correlation time (frames)	92	48	46	33	10
Correlation time (s)	0.31	0.16	0.16	0.11	0.034
Column					
Correlation time (frames)	250	94	-	78	19
Correlation time (s)	0.84	0.32	-	0.26	0.064

Table 12. Correlation times for location variables for Lonsdale with filter.

	f5f1222	f5h1225	f5q1227	f5e1229	f5s1231
Row					
Correlation time (frames)	61	-	-	-	-
Correlation time (s)	0.21	-	-	-	-
Column					
Correlation time (frames)	6	-	-	-	-
Correlation time (s)	0.020	-	-	-	-

Table 13. Correlation times for location variables for O'Sullivan's Beach.

	nf1508	nh1510	nq1512	ne1514	ns1516
Row					
Correlation time (frames)	22	23	16	9	-
Correlation time (s)	0.074	0.077	0.054	0.030	-
Column					
Correlation time (frames)	121	60	21	5	-
Correlation time (s)	0.41	0.20	0.071	0.017	-

## 5.8 Absolute values of parameters

In order to relate the results obtained here to other sensor systems, and to be able to generate synthetic target data, the magnitudes of the quantities need to be expressed in absolute values. The aperture averaging factor of 0.89 as discussed in Section 2.1 was applied to the standard deviation:mean ratios of scintillation strength. The average standard deviations of the image motions and PSF widths for the two sites are given in angular units in Tables 14 and 16. It can be seen that the image motions are a small fraction of the PSFs. It is also apparent that the camera integration time, 1.4 to 3 ms, was much shorter than the correlation time, so the camera would have produced isolated snapshots of the scintillation.

In Tables 14 and 16 the values for the unattenuated sequences are given, except where there was an obvious rogue value. The standard deviation/mean ratios were calculated from the log radiance distributions, and these values were used to calculate the standard deviations. The width of the PSF is given by the standard deviation of a Gaussian fitted to a section through the PSF. The magnitude of the scintillation given by the ratio of standard deviation to mean is summarised in Table 14. The regime of weak turbulence is specified by Ziesse as occurring below a maximum standard deviation to mean ratio of 2.3 [2]. The observed scintillation therefore occurred well within the weak region.

As noted previously the column locations were not corrected for any possible image motion and may not be as accurate as the row locations. Since row and column locations were uncorrelated the row values will be used to indicate the magnitude of the image motion. There was considerable scatter of the correlation times for the widths and locations. Since these are derived quantities they are subject to greater uncertainty. The measurement procedure in future should be optimised to reduce extraneous vibrations, and integration times should be optimised to give the best possible signal to noise ratios.

Table 14. PSF Parameters

	Lonsdale, no filter	Lonsdale, filter	O'Sullivan's Beach
Mean maximum Radiance ( $\text{Wm}^{-2}\text{sr}^{-1}$ )	2.89	0.19	1.17
Standard deviation of Radiance ( $\text{Wm}^{-2}\text{sr}^{-1}$ )	1.06	0.081	0.69
Standard deviation/Mean	0.42	0.52	0.72
Atmospheric PSF width (mrad)	0.049	0.046	0.050
Standard deviation of width (mrad)	0.0087	0.0135	0.0097
Standard deviation of row motion (mrad)	0.011	0.018	0.009
Standard deviation of column motion (mrad)	0.015	0.014	0.019

Table 15. Mean radiances and standard deviations of the standardised background images.

	Lonsdale, no filter	Lonsdale, filter	O'Sullivan's Beach
Mean Radiance ( $\text{Wm}^{-2}\text{sr}^{-1}$ )	0.166	0.073	0.182
Standard deviation ( $\text{Wm}^{-2}\text{sr}^{-1}$ )	0.003	0.001	0.005

Table 16. Correlation times of the PSF parameters.

	Lonsdale, no filter	Lonsdale, filter	O'Sullivan's Beach
Maxima (s)	0.146	0.027	0.060
Width (s)	0.074	na	0.24
Row location (s)	0.31	0.21	0.074
Column locations (s)	0.84	0.02	0.41

## 5.9 Effect of meteorological conditions

The standard theory of the interaction of meteorology and scintillation identifies the main factors which produce scintillation as the air-sea temperature difference (ASTD) and the wind velocity perpendicular to the line of sight [1]. Qualitatively, a negative ASTD due to warm sea and cool air causes unstable conditions, with convection currents and regions with different refractive indices. The greater the negative ASTD the greater the expected magnitude of scintillation. There is no such obvious mechanism for neutral and stable conditions. The temporal variation of scintillation is assumed to be due to the wind blowing the regions of variable refractive index across the line of sight.

The ASTD was measured at sites near the source and near the camera. At the source it varied from  $-2.0^{\circ}\text{C}$  at 1030 hrs to  $-1.1^{\circ}\text{C}$  at 1530 hrs, and at the camera from  $-1.6^{\circ}\text{C}$  at 1130 hrs to  $-0.7^{\circ}\text{C}$  at 1355 hrs. There was an increase of  $0.9^{\circ}\text{C}$  at both sites over the time of the measurements. The measured wind speeds were in the range 1.6 to 1.9 m/s at 1030 hrs, 4.2 to 6.1 m/s at 1230 hrs and 5 to 5.5 m/s at 15.30. The direction was

generally southwesterly, which was close to the camera-source line of sight. The wind direction was also from over the water, so land based turbulence was not being blown across the line of sight.

The scintillation strength values for the Lonsdale site were similar; 0.42 for the unfiltered case, and 0.52 for the filtered case. These values were considerably lower than the value for the O'Sullivans Beach site; 0.72. The measurements at the Lonsdale site were made at about 1030 and 1230 hrs, and at the O'Sullivans Beach site at about 1500 hrs. The lower ASTD for the O'Sullivans Beach measurements would be expected to have led to lower scintillation, but the opposite trend was observed.

The wind speed was very low during the Lonsdale unfiltered measurements, which may explain the long correlation time. The correlation time dropped significantly for the runs at Lonsdale at 1230 hrs and O'Sullivans Beach, where the wind speed had increased significantly. This result suggests that the idea that the way the wind blows the regions of different refractive index across the line of sight may explain some of the temporal behaviour. It may also be the case that the increased wind generated more turbulence in a direct fashion.

These results confirm the overseas experience that the relation between scintillation and meteorological conditions is complex and not fully understood.

Further measurements are required over the types of meteorological conditions encountered in service to obtain a representative range of model parameters.

## 5.10 Consequences of scintillation and atmospheric blurring for IRST systems

The optical and FPA parameters of the IR camera and lens used to obtain the data were similar to the expected parameters of future staring IRST systems. The scintillation and atmospheric effects should therefore be similar in both. It would be expected that errors in the estimates of scintillation parameters would tend to cancel if the camera data was used to predict IRST system performance.

The width of the combined optics and atmosphere PSF as given by the standard deviation of the fitted Gaussian was 0.058 mrad, or 0.58 of the IFOV. Most of the width of the PSF was due to the effect of atmosphere.

The IFOV is an important parameter in the design of an IRST sensor. A larger IFOV is desirable because it allows a greater overall field of view for the same size FPA. However, a smaller IFOV increases the detection ability of the sensor. At horizon ranges the geometric projection of an anti-ship missile on the FPA corresponds to a few percent of the area of a pixel. This means that the signal to noise ratio is very low, and decreases with increasing IFOV. In addition, the images are usually filtered with some form of spatial filter in order to enhance the response from point targets and minimise

the response from extended targets. The smaller the IFOV the greater the ability to discriminate point targets.

However, the benefit of decreasing the IFOV is limited because of the finite size of the PSF of the target. For very large IFOVs, (much larger than the target PSF), the relative contribution of the target energy to the total energy integrated over the pixel is small. Hence decreasing the IFOV would have a strong positive effect on signal-to-noise ratio (SNR). As the IFOV is decreased to less than the size of the PSF, more of the target energy falls on adjacent pixels. Decreasing the IFOV still increases the SNR, but by ever smaller amounts. The background radiance is assumed to be constant, but the radiance of the target PSF increases to a maximum at the centre. Assuming the PSF is centred in the IFOV, the smaller the IFOV the greater the relative integrated target radiance for a constant background radiance, and the greater the SNR. However, near the maximum of the PSF the shape becomes flat and the effect of decreasing IFOV is diminished. In the current case, about 40% of the energy would be detected by a pixel for a centred PSF and the effect of decreasing the IFOV further would be small.

The effect of image location in a pixel on the observed radiance magnitude was illustrated for the calculated values shown in Figure F2 and for the observed values in Figure F1 in Appendix F. The amount of reduction of response, from the value at the centre of the pixel, is non-linear with distance, and attains a value of about  $1/1.4 \sim 0.7$  for a displacement of 0.5 pixels. The standard deviation of the image motion caused by the atmosphere was about 0.015 mrad, or 0.15 pixels, so the effect of motion is not large, but it is still significant. Because of the non-linear response, the effect would be greater for off centre images. It is likely that image jitter from inadequate stabilisation would cause displacements up to 0.5 pixels, and hence reductions of radiance of 30%.

The radiance magnitude correlation times ranged from 0.15 s down to 0.03 s, or 7 to 1.5 frames at a frame rate of 50 frames/s. At the shorter correlation time there should be sufficient change between frames for a detection method based on frame difference to give adequate performance, but at the longer correlation times the efficiency of this type of algorithm may be reduced.

## 6. Conclusions

Measurements have been made of the scintillation of a point IR source caused by atmospheric turbulence over a horizontal path of approximately 20 km over water off the coast of Adelaide. The meteorological conditions varied during the measurements: the air-sea temperature difference (ASTD) changed from  $-2^{\circ}\text{C}$  to  $-1.1^{\circ}\text{C}$ , and the wind speed changed from approximately 1.6 m/s to approximately 5 m/s during the period 1030 hrs to 1530 hrs. The radiance fluctuations followed the log-Gaussian distribution over the range of radiances measured. The magnitude of the fluctuations, as given by the ratio of the standard deviation to the mean, increased from 0.42 to 0.72 over the

period when the negative ASTD decreased from  $-2^{\circ}\text{C}$  to  $-1.1^{\circ}\text{C}$ . This variation was opposite to the expected trend. However, the wind speed increased over this period, so the wind may have generated more turbulence directly and partially compensated for the effect of ASTD.

The correlation time of the radiance fluctuations decreased from 0.146 s to 0.060 s over the period when the wind speed increased with increasing wind speed as would be expected.

A phenomenological model of scintillation was proposed, and the data was analysed to derive values for the parameters of the model and their temporal correlations. The parameters were the maximum and width of the atmospheric point spread function (PSF) and its apparent motion. The correlation times for each of the parameters were different, and the parameters were independent of each other. The analysis included corrections for the PSF of the optics and the finite size effects of the pixels on the focal plane array. Further measurements are required over the types of meteorological conditions encountered in service to obtain a representative range of model parameters.

Some of the measurements were affected by extraneous vibrations, and corrections applied to minimise their effect. Future measurements should be made using vibration-proof mountings for the camera.

The effect of the results on the design of some aspects of staring IRST systems were discussed. The size of the atmospheric PSF suggested a maximum effective resolution for IRST optics. Stabilisation errors in the IRST sensor would cause significant apparent scintillation.

## 7. Acknowledgements

The author would like to acknowledge valuable assistance with the IR measurements from Mr. Stephane Collignon and Mr Greg Teague. Mrs Jane Mitchell kindly provided access to the Henley Sailing Club premises. The National Tidal Authority provided meteorological data.

## 8. References

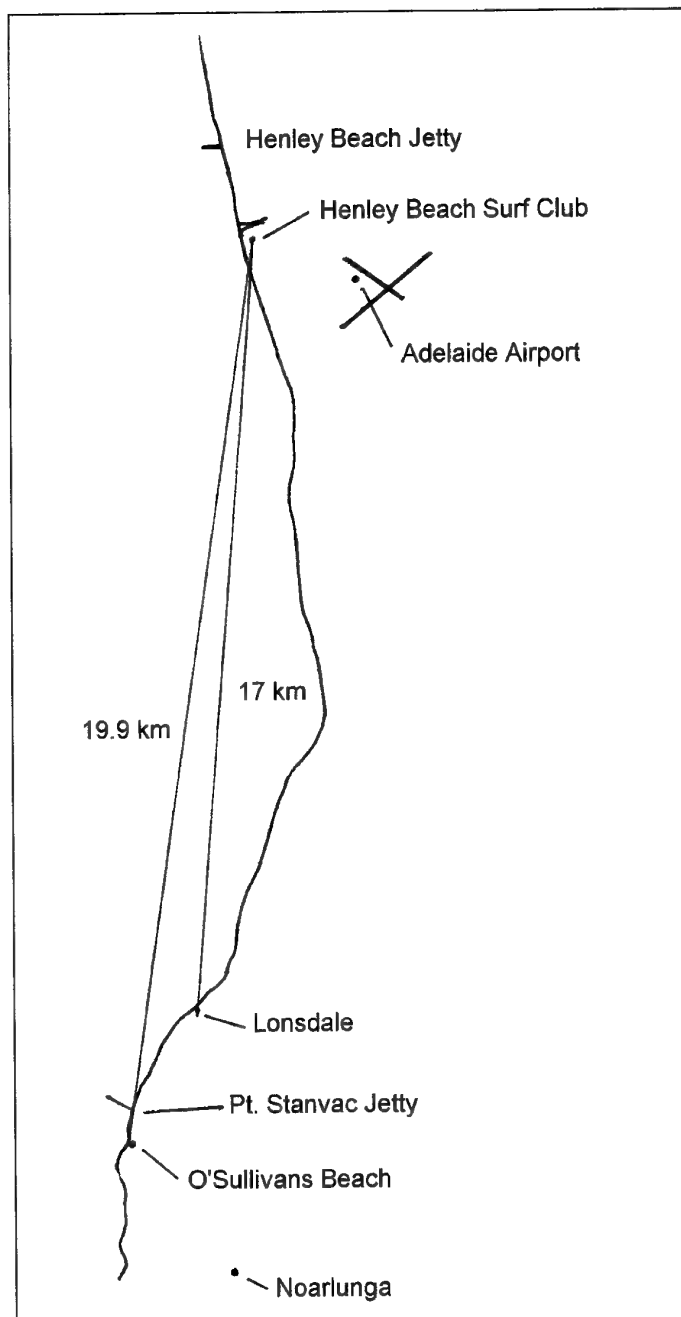
- 1 Hufnagel, R. E. (1985) Propagation through atmospheric turbulence. In: Wolfe, W. L. and Zissis, G. J. (eds) *The Infrared Handbook*. Office of Naval Research, Washington, D.C., pp. Chap. 6.
- 2 Zeisse, C. R., Nener, B. D. and Dewees, R. V. (2000) Measurement of low-altitude infrared propagation, *Applied Optics*. 39(6) 873-886

- 3 Churnside, J. H. (1991) Aperture averaging of optical scintillations in the turbulent atmosphere, *Applied Optics* 30(15) 1982-1994
- 4 de Jong, A. and Winkel, H. (1997) Point target extinction and scintillation as function of range at LAPTEX, Crete, *Propagation and Imaging through the Atmosphere* SPIE 3125, Bissonnette, L. R. and Dainty, C. (eds) SPIE - International Society for Optical Engineering.
- 5 Frederickson, P., Davidson, K., Zeisse, C. and Bendall, I. (1998) A Comparison of near-surface bulk and scintillation  $C_n^2$  measurements during EOPACE, *Propagation and Imaging through the Atmosphere II* SPIE 3433, Bissonnette, L. R. (ed) SPIE - International Society for Optical Engineering.
- 6 de Jong, A. and de Leeuw, G. (1997) Low elevation transmission measurements at EOPACE; Part III: Scintillation effects, *Propagation and Imaging through the Atmosphere* SPIE 3125, Bissonnette, L. R. and Dainty, C. (eds) SPIE - International Society for Optical Engineering.
- 7 de Jong, A., Roos, M., Winkel, H., Fritz, P., de Leeuw, G., Frederickson, P. and Davidson, K. (1998) Scintillation measurements during the EOPACE November '96 and August '97 campaigns, *Propagation and Imaging through the Atmosphere II* SPIE 3433, SPIE - International Society for Optical Engineering.
- 8 Schwering, P. and Kunz, G. (1995) Infrared scintillation effects over sea, *Atmospheric Propagation and Remote Sensing IV* SPIE 2471, Dainty, C. (ed) SPIE - International Society for Optical Engineering.
- 9 Kunz, G. I., Moerman, M. M., Fritz, P. J. and Leeuw, G. d. (1996) Validation of a bulk turbulence model with thermal images of a point source, *Image Propagation through the Atmosphere* SPIE 2828, Dainty, C. and Bissonnette, L. R. (eds) SPIE - International Society for Optical Engineering.
- 10 Kohnle, A., Neuwirth, R., Sehuberth, W., Stein, K., Höhn, D. H., Gabler, R., Hofmann, L. and Euing, W. (1993) Evaluation of essential design criteria for IRST systems, *Infrared Technology XIX* SPIE 2020, Andresen, B. F. and Shepherd, F. D. (eds) SPIE - International Society for Optical Engineering.
- 11 Doob, J. L. (1942) Topics in the theory of Markov chains., *Trans.Amer. Math. Soc.* 52(37-64)
- 12 Payne, T. (1996) Apparent scintillation of sub-pixel targets imaged by focal plane arrays, *Infrared Imaging Systems: Design, Analysis, Modeling, and Testing VII* SPIE 2743, Holst, G. C. (ed) SPIE - International Society for Optical Engineering.

- 13 Poropat, G. V. (1998) Effect of system point spread function, apparent size, and detector instantaneous field of view on the infrared image contrast of small objects, *Optical Engineering* **32**(10) 2598-2607
- 14 Tidhar, G. (1999) IR FPA phase noise effects in IRST design, *Infrared Technology and Applications XXV* SPIE 3698, Andresen, B. F. and Strojnik, M. (eds) SPIE - International Society for Optical Engineering.
- 15 Ronda, V., Deshpande, S. D., Yoganandam, Y. and Gan, Y.-H. (1999) Fill-factor of FPA: effect on image registration and tracking, *Infrared Imaging Systems: Design, Analysis, Modelling, and Testing X* SPIE 3701, Holst, G. C. (ed) SPIE - International Society for Optical Engineering.

DSTO-RR-0231

## Appendix A: Site map





## Appendix B: Meteorological Conditions

Table B.1. Air and sea temperatures at Henley Jetty

Time	11.30	13.55
Air Temperature (°C)	22.6	23.4
Sea Temperature (°C)	24.2	24.1
ASTD (°C)	-1.6	-0.7

Table B.2. Meteorological conditions at Pt. Stanvac

Time	10.30	11.30	12.30	13.30	14.30	15.30
Air Temperature (°C)	20.5	20.5	20.7	21	21.3	21.7
Sea Temperature (°C)	22.5	22.6	22.7	22.6	22.9	22.8
ASTD (°C)	-2	-2.1	-2	-1.6	-1.6	-1.1
Wind Speed (m/s)	1.6	3.7	4.5	5.4	5.6	5.5
Wind Gust (m/s)	3.3	4.4	5.9	6.1	6.5	6.2
Wind direction (°)	181	189	185	179	186	175
Tide (m)	1.181	0.796	0.448	0.265	0.267	0.476

Table B.3. Meteorological conditions at Adelaide Airport

Time	10.30	11.30	12.30	13.30	14.30	15:30
Pressure (hPa)	1018.7	1018.6	1018.3	1017.6	1017.9	1017.5
Air Temperature (°C)	22.2	24	23.5	25	25	25.5
Wind Speed (m/s)	1.9	3.1	6.1	6.1	6.1	5.0
Wind Gust (m/s)	3.6	4.7	7.8	7.8	7.2	6.7
Wind direction	SW	SW	SW	SW	SW	SW
Dew point (°C)	9.8	11.8	12.7	14	13.4	10.8
Relative humidity (%)	45	46	51	50	49	40

Table B.4. Meteorological conditions at Noarlunga

Time	10.30	11.30	12.30	13.30	14.30	15.30
Air Temperature (°C)	21.8	23.6	23.1	24.2	24.7	24.8
Wind Speed (m/s)	1.7	3.6	4.2	4.2	4.7	5.0
Wind Gust (m/s)	3.1	5.0	5.6	5.6	6.1	6.7
Wind direction	W	W	WSW	SW	WSW	SW
Dew point (°C)	10	12	11.8	12.2	12.6	12.1
Relative humidity (%)	47	48	49	47	47	45



## Appendix C: Data Recording Details

	Code	Integration time (ms)	Frame Rate (s <sup>-1</sup> )	Number of frames
Lonsdale, No filter	Bg1019	1.4	296	5000
	Nf1025	1.4	297	20000
	Nh1027	1.4	297	20000
	Nq1029	1.4	296	20000
	Ne1031	1.4	297	20000
	Ns1033	1.4	297	20000
Calibration.	251118	1.4	280	1000
	401122	1.4	280	1000
	551125	1.4	280	1000
Lonsdale, Filter 4.42-5.46μ	Bgf51209	2.5	296	5000
	F5f1222	3	248	20000
	F5h1225	3	248	20000
	F5q1227	3	248	20000
	F5e1229	3	248	20000
	F5s1233	3	248	20000
Calibration	251155	2.5	288	1000
	401150	2.5	288	1000
	551144	2.5	288	1000
O'Sullivans Beach	Nf1508	1.4	297	5000
	Nh1510	1.4	297	20000
	Nq1512	1.4	297	20000
	Ne1514	1.4	297	20000
	Ns1516	1.4	297	20000
	Bgnf1522	1.4	297	5000



## Appendix D: Parameters of Raw Radiance Distributions

The values of the mean and the standard deviation of the log distribution of the signal maximum and total from the Lonsdale site with no filter are given in Table D1. Table D.1 also gives the values of the log standard deviation calculated directly from the radiance distribution.

Table D.1. Parameters of the distributions of radiances at Lonsdale, no filter.

Run number	nf1025	nh1027	nq1029	ne1031	ns1033
	1	2	3	4	5
Maximum					
Log Mean	0.38	-0.25	-0.85	-1.59	-2.08
Log Standard deviation	0.37	0.40	0.40	0.432	0.39
Correlation Coefficient	0.996	0.994	0.990	0.983	0.972
Standard deviation/mean, Gaussian	0.39	0.42	0.42	0.453	0.40
Standard deviation/mean, direct	0.37	0.36	0.38	0.401	0.38
Total					
Log Mean	1.65	1.01	0.39	-0.20	-0.86
Log Standard deviation	0.34	0.37	0.38	0.377	0.36
Correlation Coefficient	0.990	0.986	0.995	0.992	0.997
Standard deviation/mean, Gaussian	0.35	0.38	0.39	0.391	0.37
Standard deviation/mean, direct	0.35	0.33	0.35	0.344	0.35

The measured parameters for the Lonsdale site with the filter are given in Table D.2. The signal magnitude was much lower with the filter, and magnitudes for the attenuators were too low to give reliable analyses of the Total data.

Table D.2. Parameters of the distributions of radiances at Lonsdale with filter.

	f5f1222	F5h1225	f5q1227	f5e1229
Maximum				
Log Mean	-2.30	-2.95	-3.51	-4.30
Log Standard deviation	0.49	0.48	0.44	0.55
Correlation Coefficient	0.986	0.97	0.948	0.936
Standard deviation/mean, Gaussian	0.52	0.51	0.46	0.59
Standard deviation/mean, direct	0.45	0.46	0.43	0.47
Total				
Log Mean	-0.21			
Log Standard deviation	0.38			
Correlation Coefficient	0.992			
Standard deviation/mean, Gaussian	0.39			
Standard deviation/mean, direct	0.34			

The measured parameters for the O'Sullivans Beach site are given in Table D3. There was more scatter in the parameters than for Lonsdale, probably due to the longer range and also the effect of camera motion.

*Table D.3. Parameters of the distributions of radiances at O'Sullivans Beach*

	nf1508	nh1510	nq1512	ne1514	ns1516
Maximum					
Log Mean	-0.63	-1.23	-1.73	-2.46	-3.17
Log Standard deviation	0.62	0.62	0.58	0.60	0.50
Correlation Coefficient	0.996	0.995	0.992	0.983	0.990
Standard deviation/mean, Gaussian	0.69	0.68	0.63	0.66	0.54
Standard deviation/mean, direct	0.55	0.57	0.52	0.53	0.50
Total					
Log Mean	0.44	-0.13	-0.52	-1.38	-1.95
Log Standard deviation	0.60	0.58	0.53	0.64	0.58
Correlation Coefficient	0.990	0.998	0.985	0.970	0.975
Standard deviation/mean, Gaussian	0.66	0.63	0.57	0.71	0.63
Standard deviation/mean, direct	0.53	0.54	0.50	0.56	0.56

## Appendix E: Correlation Times of Radiance Fluctuations

The temporal correlation of the image maxima was calculated from the correlation coefficient between the sequence and the same sequence shifted by progressively increasing number of frames. The correlation time was taken to be the time for the correlation to fall to a value of  $1/e$ . To test the variability during a run, the 20000 frames of the sequence were broken up into 5 lots of 4000 frames. There was some scatter between lots, but it was not significant. The correlation time varied between 0.027 s and 0.147 s.

Table E.1. Temporal correlation of radiance at Lonsdale, no filter.

	Correlation time (frames)					Correlation	
	nf1025	nh1027	nq1029	ne1031	ns1033	Overall	time (s)
Maximum							
Mean	37.6	53.6	45	43.6	37.4	43.4	0.146
Standard deviation	3.9	11.6	6.4	5.7	4.2		
Total							
Mean	38.8	51.4	50.4	43	35	43.7	0.147
Standard deviation	4.1	10.9	9.5	3.8	3.3		
Frame rate	297						

Table E.2. Temporal correlations of radiance at Lonsdale, filter.

	Correlation time (frames)			Correlation			
	f5f1222	f5h1225	f5q1227	-	-	Overall	time (s)
Maximum							
Mean	7.2	7	6.8	-	-	7	0.028
Standard deviation	0.4	0	0.4	-	-		
Total							
Mean	7	6.6	6.4	-	-	6.7	0.027
Standard deviation	0	0.5	0.5	-	-		
Frame rate	248						

*Table E.3. Temporal correlation of radiance at O'Sullivan's Beach*

	Correlation time (frames)					Overall	Correlation time (s)
	nf1508	nh1510	nq1512	ne1514	ns1516		
Maximum							
Mean	17.8	15.4	16.8	19.3	17.2	17.3	0.058
Standard deviation	1.1	1.3	1.5		1.3		
Total							
Mean	19.4	15.2	17.8	20	19.4	18.4	0.062
Standard deviation	2.2	0.8	1.6		2.2		
Frame rate	297						

## Appendix F: Calculation of the Effects of Finite Pixel Size

The measurement of scintillation with a focal plane array (FPA) camera is complicated by the discrete nature of the sensing elements. There are two effects on the observed radiance, the reduction in pixel value caused by the PSF overlapping adjacent pixels which is exacerbated when the source is not imaged in the centre of a pixel, and the fact that the observed radiances are the result of integration of the PSF over the sensitive areas of the individual pixels. The off-centre effect will be discussed first.

In the case of the Galileo camera the pixel spacing is  $30\mu\text{m}$  on side and the sensitive area is  $27\mu\text{m}$  on side, giving a fill factor of 80 %. The 85% energy spot diameter of the optics is  $35.6\mu\text{m}$ , which is of the same order as the pixel size. If the image of a point is centred on the pixel then most of the energy should fall on that pixel, and little on adjacent pixels. The fact that the PSF is comparable in size to the pixel can be used to simplify the analysis to obtain estimates of scintillation parameters.

The observed radiance will be affected by the position of the image relative to the pixel centre. The PSF centre can vary up to  $\pm 0.5$  pixel spacings in the row and column directions within the pixel where it was detected, or else it would be detected in an adjacent pixel. If the size of the image is much smaller than the pixel, the response will be approximately constant for locations over the sensitive area of the pixel, but near zero in the dead areas between pixels. For the case where the PSF of the point source is comparable to the pixel size, when the image is off centre the response of the pixel containing the centre of the source image is reduced and the response of adjacent pixels is increased. If there is camera motion due to jitter in the mounts, or other causes, there would be apparent scintillation on top of any atmospheric scintillation. Image motion caused by the atmosphere would also add to this effect. If the PSF is much larger than the pixel the effect of image location on response will be minimal.

Corrections to the raw data values of PSF height and width for the effect of the PSF being off pixel centre were calculated in Section 5.1. The ratios of the corrected PSF maxima to the observed values are plotted as a function of the distance of the maximum from the pixel centre for run nf1508 are shown in Figure F1. Plots for the other sequences are similar. There appears to be a definite relationship between the ratio and distance, but there is some scatter. The nature of this relation is discussed below.

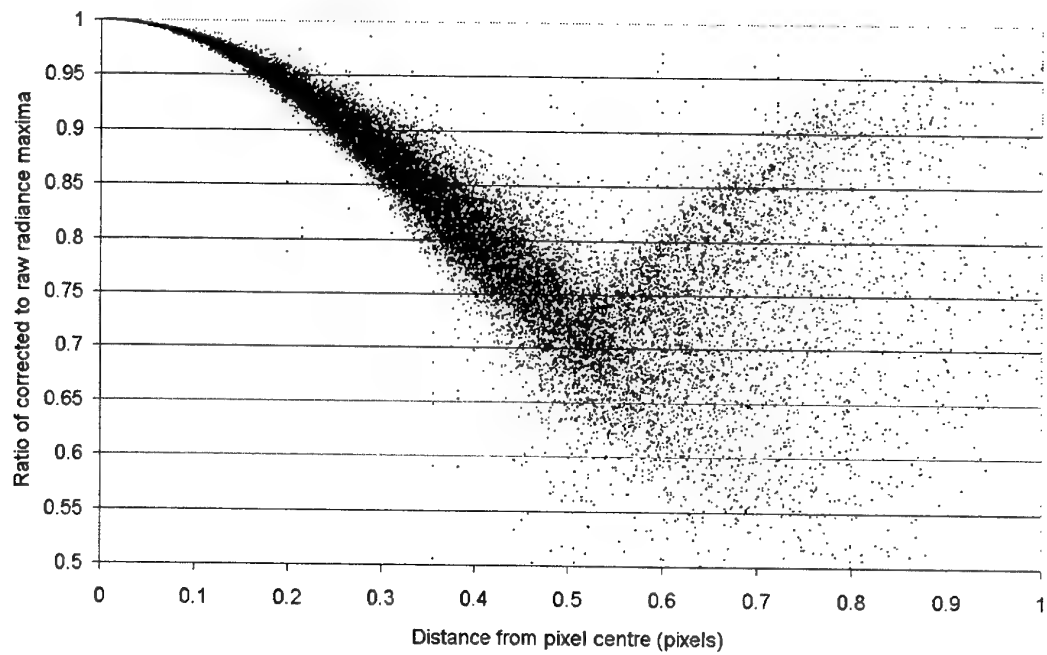


Figure F1. Ratio of corrected to raw radiance maxima vs distance from pixel centre for nf1508

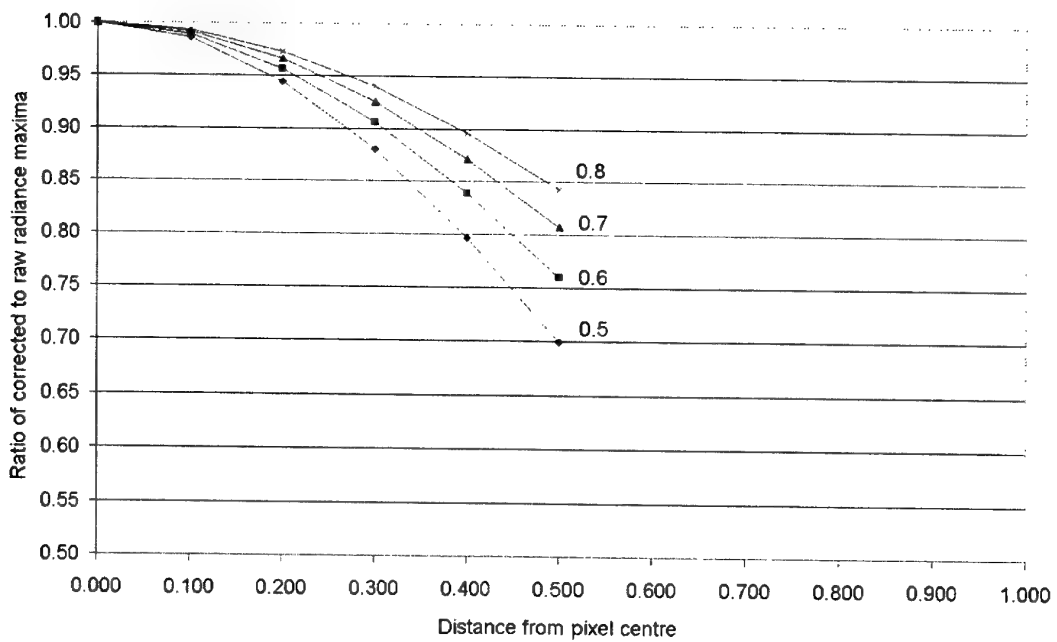


Figure F2. Calculated relative radiance maxima vs distance of maxima from pixel centre. Standard deviation of distribution given by the figures.

The relationship between measured radiance and distance of the image centre from the pixel centre will be derived for a hypothetical Gaussian PSF on a linear set of 3 pixels.

The standard deviation of the combined atmospheric and optics PSF from Table 4 was in the vicinity of 0.6, so the hypothetical PSF will be defined to have a maximum in the centre pixel of 1.0 and standard deviation 0.6. This function was integrated numerically over the ranges -1.5 to -0.5, -0.5 to 0.5, and 0.5 to 1.5, representing pixels at -1, 0, and 1 pixel units. The calculated pixel values are given in Table F1 under the heading 0. The integral over the middle pixel gave a value of 0.895, and the adjacent pixels gave values of 0.295. Table F1 gives the results of similar calculations when the position of the peak of the PSF is shifted 0.1, 0.2, 0.3, 0.4 and 0.5 pixels.

If the source image was centred in a pixel, the ratio of integrated to true values of the maxima would be 0.895. From Table F1 it can be seen that as the source moves from the centre the integrated ratio progressively decreased to 0.680.

*Table F1. Integrated values of Gaussian PSFs over pixel areas.*

Shift	0	0.1	0.2	0.3	0.4	0.5
Pixel offset	Integral values in 1 pixel wide swathes					
-1	0.295	0.233	0.180	0.135	0.099	0.071
0	0.895	0.885	0.857	0.811	0.751	0.680
1	0.295	0.365	0.441	0.521	0.602	0.680

The calculated ratios, normalised to 1 at zero shift, are shown in Figure F2. The calculations were repeated for standard deviations of 0.5, 0.7 and 0.8, and these results are shown as well on Figure F2. For comparison in Figure F1 most of the points below a distance of 0.5 fall in a band showing strong similarity to the calculated curve in Figure F2. Above a distance from the centre of 0.5 pixel spacings the points become very scattered. For shifts above 0.5 pixels there would be increasing ambiguity in the calculations as to which pixel the maximum was associated with, as the maximum distance from the centre along an axis is 0.5, and 0.7 along a diagonal. It can be seen that there is a small trend to mirror the distribution above 0.5 units. The figure shows that for most of the data, particularly for distances less than 0.5, that there is a relation between the ratio of maxima and distance similar to the theoretical relation. The results are similar in the other image sequences. This result gives confidence that the correction procedure for off centre location is approximately correct.

A further correction is required to the measured radiance values. The experimental radiance measurements are integrals of the continuously variable true PSF over the sensitive areas of the pixels of the FPA. To obtain the true PSF a transformation is required from the measured, integrated values to the original PSF. The way to calculate this effect is not obvious. One way would be to fit a 2D PSF to the radiance values of the pixels containing the source image, but this approach is not practical for a number of reasons. The exact form of the PSF is not known, and the radiance values are very coarse and noisy, so any fit procedure is likely to be unstable. It is conceptually simpler to reverse the procedure and calculate the integrated values from a standard

hypothesised PSF and then use these to calculate a correction to the original integrated values.

The forgoing analysis indicates that a true Gaussian PSF with maximum 1.0 and standard deviation of 0.6 pixels centred on a pixel would give integrated radiance values of 0.295, 0.895 and 0.295 on 3 linearly adjacent pixels (Table F1). Treating these values as observed pixel radiances, a Gaussian fitted to these data would give a maximum of 0.895 and a standard deviation of 0.671. Table F2 gives the results of the same procedure for different shifts of the hypothetical centre of the PSF from the pixel centre and for different hypothetical standard deviations. It can be seen that for a given hypothetical standard deviation the results are virtually independent of shift over the range calculated. This means for a measured standard deviation of 0.6 that fitting a Gaussian to the observed radiances would underestimate the true value of the maximum by a factor of  $1/0.895 = 1.117$ , and overestimate the standard deviation by a factor of  $0.716/0.65 = 1.118$ . Similar factors apply for other measured standard deviations.

The fact that when the standard deviation is decreased by a given factor the maximum value is increased by the same factor is encouraging because it means that the process conserves the area of the distribution. However, while the fit has been made on a 1D section through the PSF, the PSF is actually 2D, and the question arises as to the correct factor to increase the maximum value for a given decrease in standard deviation. If the standard deviation decreases in one direction it is also assumed to decrease in the other direction by the same amount, so the effect on the maximum in 2D is twice the effect in 1D. Numerical integrations of typical cases confirm this. The overall calculated factors to apply to the measured PSFs calculated by the above procedure are given in Table F3. The values are not very sensitive to the shift, so the values for zero shift will be used. Intermediate values between standard deviations were calculated from a quadratic fit.

The probability distribution for the width parameter was not a simple Gaussian as it was skewed in the low value direction, but it was reasonably approximated by a log Gaussian distribution. Figure F3 shows the distribution and a fitted log Gaussian for nf1025, and the other cases were similar. For simplicity, a simple Gaussian will be assumed for the model. The estimated parameters of the true radiance PSF falling on the FPA for the image sequences are given in Table F4-F6. The standard deviation of the width was calculated from the log width parameters, because the few outlying width values would have distorted a direct calculation. The values for the maximum are the final values to be used in the phenomenological model, but the width values will be corrected for the optics PSF.

Table F2. Parameters of fitted Gaussian functions.

Shift	0	0.1	0.2	0.3	0.4	0.5
<b>Standard deviation =0.5</b>						
Maximum	0.855	0.856	0.859	0.864	0.870	0.875
Location of maximum	0.000	0.103	0.205	0.305	0.404	0.500
Standard deviation	0.584	0.584	0.582	0.580	0.577	0.573
<b>Standard deviation =0.6</b>						
Maximum	0.895	0.895	0.896	0.898	0.900	0.901
Location of maximum	0.000	0.101	0.202	0.302	0.402	0.500
Standard deviation	0.671	0.671	0.670	0.669	0.668	0.666
<b>Standard deviation =0.7</b>						
Maximum	0.921	0.921	0.921	0.922	0.922	0.923
Location of maximum	0.000	0.100	0.201	0.301	0.400	0.500
Standard deviation	0.761	0.761	0.761	0.760	0.760	0.759
<b>Standard deviation =0.8</b>						
Maximum	0.938	0.938	0.938	0.938	0.939	0.939
Location of maximum	0.000	0.100	0.200	0.301	0.400	0.500
Standard deviation	0.854	0.854	0.853	0.854	0.853	0.852

Table F3. Correction factors for the integration effect on PSF.

Shift	0	0.1	0.2	0.3	0.4	0.5
<b>Standard deviation =0.5</b>						
Factor for maximum	1.339	1.336	1.328	1.315	1.299	1.286
Factor for standard deviation	0.855	0.856	0.859	0.864	0.870	0.875
<b>Standard deviation =0.6</b>						
Factor for maximum	1.235	1.235	1.232	1.227	1.222	1.220
Factor for standard deviation	0.895	0.895	0.896	0.898	0.900	0.901
<b>Standard deviation =0.7</b>						
Factor for maximum	1.172	1.172	1.172	1.169	1.169	1.167
Factor for standard deviation	0.921	0.921	0.921	0.922	0.922	0.923
<b>Standard deviation =0.8</b>						
Factor for maximum	1.132	1.132	1.132	1.132	1.130	1.130
Factor for standard deviation	0.938	0.938	0.938	0.938	0.939	0.939

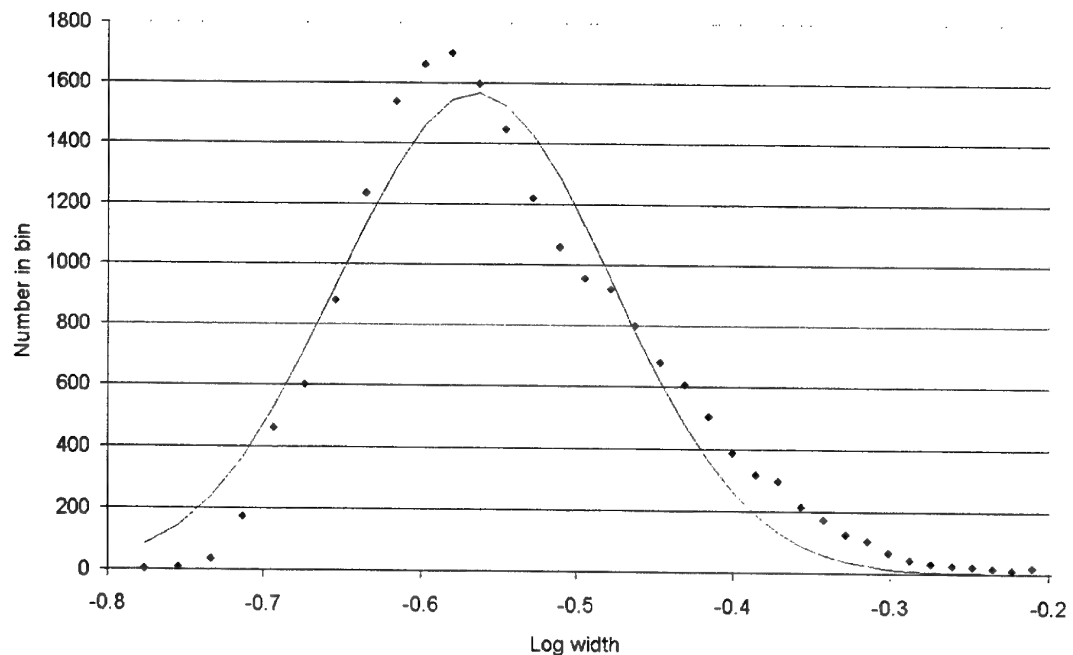


Figure F3. Histogram of the log width of the PSF of Lonsdale, no filter nf1025.

Table F4. Mean true maximum radiance and mean PSF width of measured image sequences for Lonsdale, no filter.

	nf1025	nh1027	nq1029
<b>Maximum</b>			
Mean radiance ( $\text{Wm}^{-2}\text{sr}^{-1}$ )	2.89	1.51	0.83
Standard deviation radiance ( $\text{Wm}^{-2}\text{sr}^{-1}$ )	1.06	0.54	0.39
(Standard deviation)/mean, direct	0.42	0.40	0.53
Log Standard deviation	0.35	0.38	0.38
(Standard deviation)/mean, calculated	0.36	0.40	0.39
Correlation coefficient	0.997	0.984	0.995
<b>Width</b>			
Mean (Pixels)	0.58	0.57	0.58
Standard deviation, calculated (Pixels)	0.087	0.095	0.087
Log Mean	-0.57	-0.60	-0.57
Log Standard deviation	0.087	0.094	0.087
Correlation coefficients	0.979	0.969	0.979

Table F5. Mean true maximum radiances and mean PSF widths of measured image sequences for Lonsdale with filter.

nf1222	
Maximum	
Mean radiance (Wm <sup>-2</sup> sr <sup>-1</sup> )	0.19
Standard deviation radiance (Wm <sup>-2</sup> sr <sup>-1</sup> )	0.08
(Standard deviation)/mean, direct	0.47
Log Standard deviation	0.41
(Standard deviation)/mean, calculated	0.42
Correlation coefficient	0.994
Width	
Mean (Pixels)	0.56
Standard deviation, calculated (Pixels)	0.14
Log Mean	-0.62
Log Standard deviation	0.13
Correlation coefficient	0.995

Table F6. Mean true maximum radiance and mean PSF widths of measured image sequences for O'Sullivan's Beach.

	nf1508	nh1510	nq1512
Maximum			
Mean radiance (Wm <sup>-2</sup> sr <sup>-1</sup> )	1.17	0.66	0.38
Standard deviation radiance (Wm <sup>-2</sup> sr <sup>-1</sup> )	0.69	0.42	0.28
(Standard deviation)/mean, direct	0.66	0.71	0.84
Log Standard deviation	0.59	0.59	0.53
(Standard deviation)/mean, calculated	0.64	0.64	0.57
Correlation coefficient	0.996	0.998	0.997
Width			
Mean (Pixels)	0.58	0.58	0.63
Standard deviation, calculated (Pixels)	0.097	0.11	0.14
Log Mean	-0.58	-0.58	-0.51
Log Standard deviation	0.097	0.11	0.14
Correlation coefficient	0.989	0.985	0.988



## Appendix G: Point Spread Functions of the Optics and Atmosphere

The combined blurring effect of the optics and the atmosphere is quantified by the measured PSFs. The PSF of the atmosphere alone could be obtained by a 2D deconvolution of the measured total PSF and the optics PSF. Detailed knowledge of the functional form of the PSFs would be required as well as the spatial function of the sensitive area of the FPA pixels. This procedure would be necessary if subtle differences in atmospheric effects, or other parameters, were being studied. In the present work it is only intended to obtain indicative estimates of the scintillation effects, and some approximate methods will be used.

For computational tractability, the PSFs have been approximated by assuming that plane sections through them can be given by Gaussians. The PSF of the optics is given by the manufacturer as diameter of the circle in the focal plane containing 85% of the energy of a point source. In order to be able to relate the optics PSF to the fitted Gaussian functions which were sections through the appropriate PSFs, it is necessary to convert the measure of 85% of the integral of a 2D distribution function derived by rotation of a Gaussian about the origin to the corresponding point on a 1D Gaussian. A Gaussian function is defined by

$$G(x) = \frac{1}{\sqrt{2\pi}} e^{\frac{-x^2}{2}}$$

The area under a 2D rotated Gaussian is given by

$$A(x) = k \int_0^x y \cdot \frac{1}{\sqrt{2\pi}} e^{\frac{-y^2}{2}} dy, \text{ where } x \text{ and } y \text{ are distances from the origin and } k \text{ is a normalising constant giving } A(\infty) = 1.$$

The function  $A(x)$  was evaluated numerically and the value of  $k$  determined. The function was then evaluated to determine the value of  $x=x'$  where  $A(x')=0.85$ . The value of  $x'$  was 1.94. Since the standard deviation of the normalised Gaussian was 1, the 85% total energy value corresponds to 1.94 standard deviations. So the standard deviation of the rotated Gaussian is (diameter of 85% circle)/(2x1.94).

The size of the 85% blur circle varied with position on the focal plane, and the values of the circle diameter, and the standard deviations of the fitted Gaussians are given in Table G1.

During recording the image of the source was positioned as near as possible to the centre of the focal plane, so the on-axis values will be used.

If the optics and atmospheric PSFs can be approximated by Gaussian functions, the variance of the combined PSF is given by the sum of the variances of the individual PSFs. Conversely, the variance of the atmospheric PSF can be obtained as the difference between the combined variance and the optics variance.

The PSF standard deviations are summarised in Table G2.

*Table G1. Optics PSF size*

Diameter of 85% circle	On-axis	Off-axis	Off-axis
		3.61°, 3.61mm	5.16°, 9.0mm
	0.0014"	0.0018"	0.0023"
	35.6μm	45.7μm	58.4μm
Standard deviation of Gaussian			
	9.2μm	11.8μm	15.1μm
	0.0307 mrad	0.0394 mrad	0.0504 mrad

*Table G2. Calculated standard deviations of point spread functions.*

	Observed (Pixels)	Observed (mrad)	Optics (mrad)	Atmosphere (Pixels))	Atmosphere (mrad)
Lonsdale no filter	0.58	0.058	0.031	0.49	0.049
Lonsdale filter	0.56	0.056	0.031	0.46	0.046
O'Sullivans Beach	0.59	0.059	0.031	0.50	0.050

## Appendix H: Correlations Between Parameters

Scatter diagrams of pairs of PSF parameters are given in the figures. It can be seen that There is no evidence of correlation between any of the parameters.

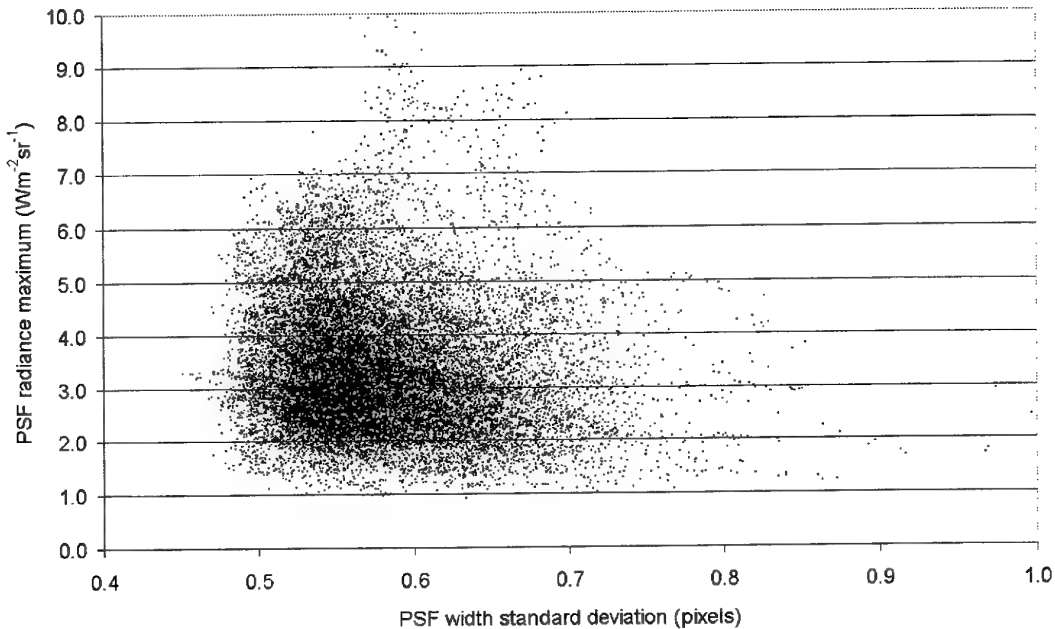


Figure H.1. Scatter diagram of PSF maximum and width for nf1025.

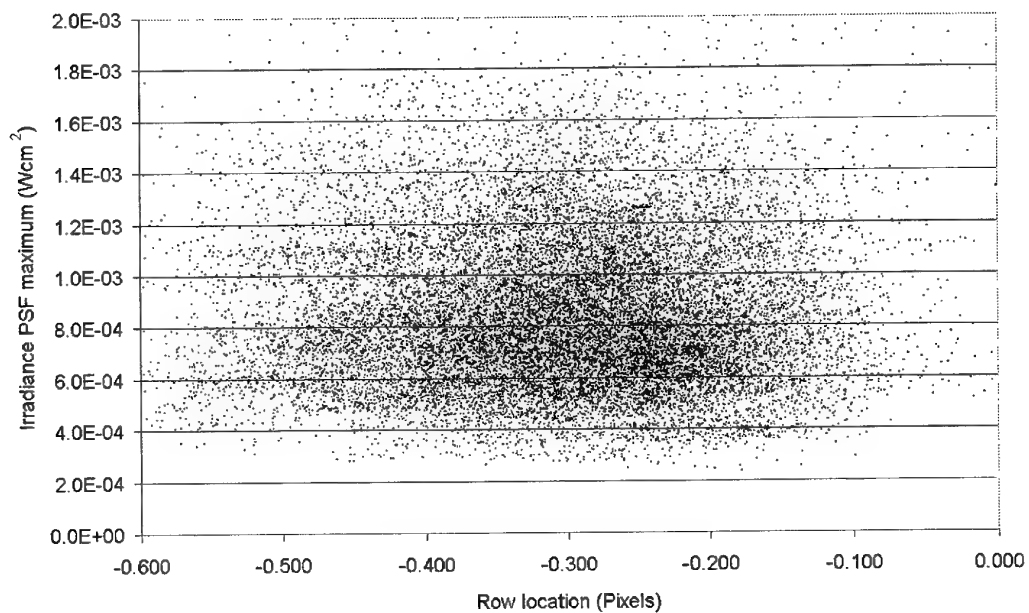


Figure H2. Scatter diagram of PSF maximum and location for nf1025

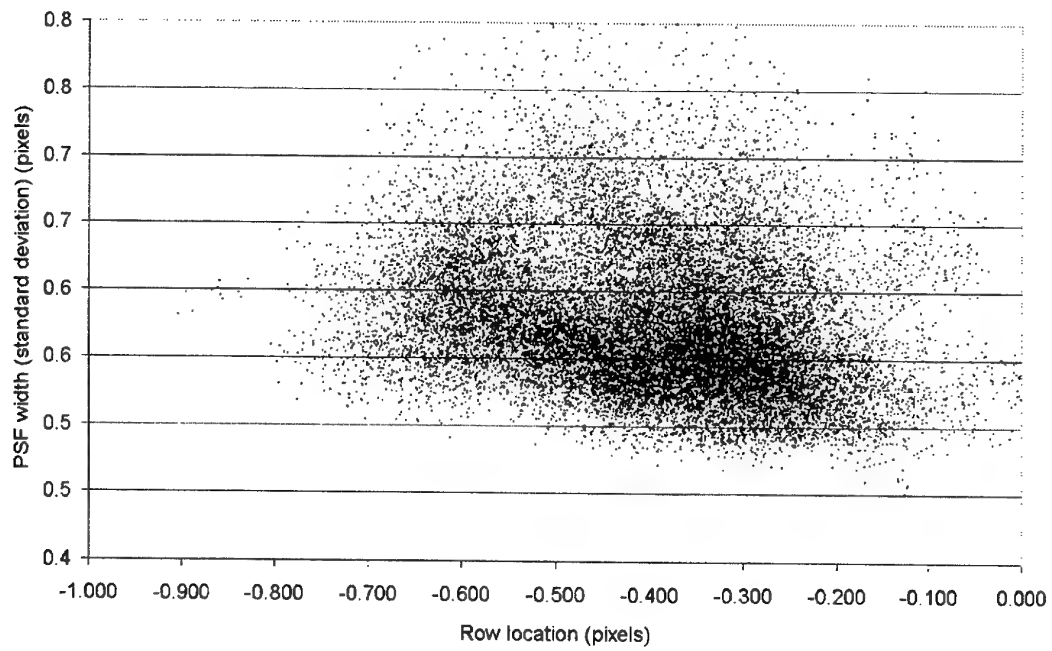


Figure H.3. Scatter diagram of PSF width and row location for nf1025.

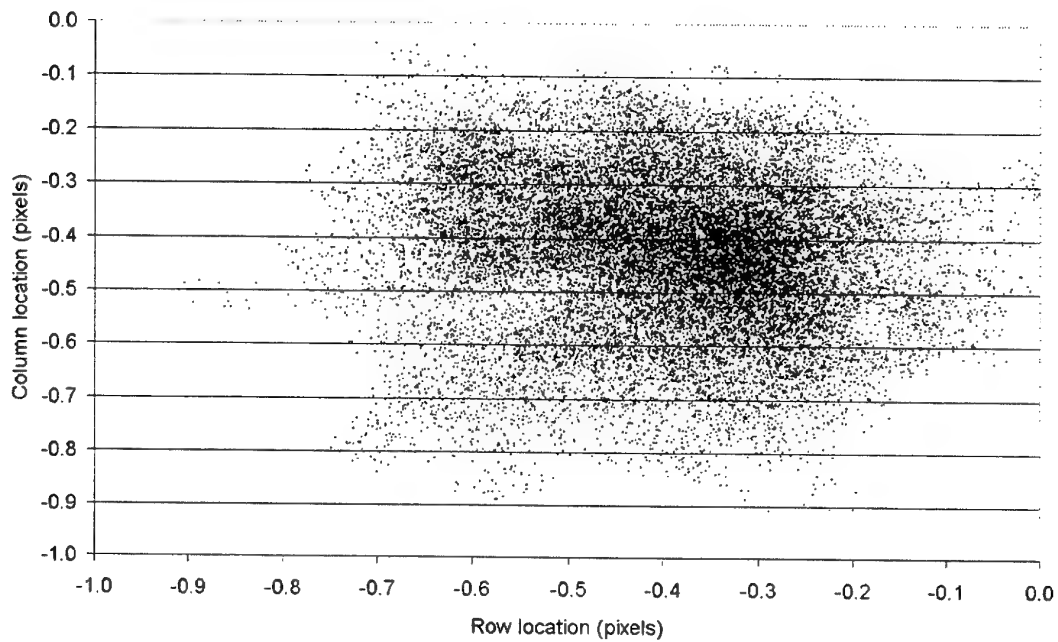


Figure H.4. Scatter diagram of row and column locations of the PSF for nf1025.

## DISTRIBUTION LIST

### A Phenomenological Model of Scintillation of Infrared Radiation from Point Targets over Water and Measurements of the Model Parameters

R. C. Warren

### AUSTRALIA

#### DEFENCE ORGANISATION

Task Sponsor                    CDRE P. Greenfield, DGMD, Russell Offices, Canberra

#### S&T Program

Chief Defence Scientist  
FAS Science Policy  
AS Science Corporate Management  
Director General Science Policy Development  
Counsellor Defence Science, London (Doc Data Sheet)  
Counsellor Defence Science, Washington (Doc Data Sheet)  
Scientific Adviser to MRDC Thailand (Doc Data Sheet)  
Scientific Adviser Joint  
Navy Scientific Adviser  
Scientific Adviser - Army (Doc Data Sheet and distribution list only)  
Air Force Scientific Adviser  
Director Trials

} shared copy

#### Aeronautical and Maritime Research Laboratory

Director

Chief of Weapons Systems Division  
Research Leader Maritime Systems  
Head Advanced Concepts Group  
Dr Stephen Carr  
Author: R.C. Warren (5 copies)

#### DSTO Library and Archives

Library Fishermans Bend (Doc Data Sheet)  
Library Maribyrnong (Doc Data Sheet)  
Library Edinburgh  
Australian Archives  
Library, MOD, Pyrmont (Doc Data sheet only)  
US Defense Technical Information Center, 2 copies  
UK Defence Research Information Centre, 2 copies  
Canada Defence Scientific Information Service, 1 copy  
NZ Defence Information Centre, 1 copy  
National Library of Australia, 1 copy

#### Capability Systems Staff

Director General Maritime Development  
Director General Aerospace Development (Doc Data Sheet only)

### **Knowledge Staff**

Director General Command, Control, Communications and Computers (DGC4)  
(Doc Data Sheet only)

### **Navy**

SO (SCIENCE), COMAUSNAVSURFGRP, BLD 95, Garden Island, Locked Bag 12, PYRMONT NSW 2009 (Doc Data Sheet and distribution list only)

### **Army**

ABCA National Standardisation Officer ( 4 copies)

Land Warfare Development Sector

Tobruk Barracks

PUCKAPUNYAL VIC 3662

SO (Science), Deployable Joint Force Headquarters (DJFHQ) (L), MILPO Gallipoli Barracks, Enoggera QLD 4052 (Doc Data Sheet only)

NPOC QWG Engineer NBCD Combat Development Wing, Tobruk Barracks, Puckapunyal, 3662 (Doc Data Sheet relating to NBCD matters only)

### **Intelligence Program**

DGSTA Defence Intelligence Organisation  
Manager, Information Centre, Defence Intelligence Organisation

### **Corporate Support Program**

Library Manager, DLS-Canberra

MS Sam Doran, Defence Library Service - Sydney West

### **UNIVERSITIES AND COLLEGES**

Australian Defence Force Academy

Library

Head of Aerospace and Mechanical Engineering

Serials Section (M list), Deakin University Library, Geelong,

Hargrave Library, Monash University (Doc Data Sheet only)

Librarian, Flinders University

### **OTHER ORGANISATIONS**

NASA (Canberra)

AusInfo

National Tidal Authority, Flinders University of South Australia (1 copy)

### **OUTSIDE AUSTRALIA**

### **ABSTRACTING AND INFORMATION ORGANISATIONS**

Library, Chemical Abstracts Reference Service

Engineering Societies Library, US

Materials Information, Cambridge Scientific Abstracts, US

Documents Librarian, The Center for Research Libraries, US

### **INFORMATION EXCHANGE AGREEMENT PARTNERS**

Acquisitions Unit, Science Reference and Information Service, UK

Library - Exchange Desk, National Institute of Standards and Technology, US

Dr G. Johnson, Naval Surface Warfare Center, Technology and Photonics Systems  
Branch, T44, 17320 Dahlgren Rd, Dahlgren, VA 22448-5100, USA

SPARES (5 copies)

**Total number of copies:** 53

<b>DEFENCE SCIENCE AND TECHNOLOGY ORGANISATION DOCUMENT CONTROL DATA</b>		1. PRIVACY MARKING/CAVEAT (OF DOCUMENT)	
2. TITLE  A Phenomenological Model of Scintillation of Infrared Radiation from Point Targets over Water and Measurements of the Model Parameters		3. SECURITY CLASSIFICATION (FOR UNCLASSIFIED REPORTS THAT ARE LIMITED RELEASE USE (L) NEXT TO DOCUMENT CLASSIFICATION)  Document (U) Title (U) Abstract (U)	
4. AUTHOR(S)  R. C. Warren		5. CORPORATE AUTHOR  Aeronautical and Maritime Research Laboratory 506 Lorimer St Fishermans Bend Victoria 3207 Australia	
6a. DSTO NUMBER DSTO-RR-0231	6b. AR NUMBER AR-012-166	6c. TYPE OF REPORT Research Report	7. DOCUMENT DATE January 2002
8. FILE NUMBER J9505/21/112	9. TASK NUMBER NAV 00/109	10. TASK SPONSOR DGMD	11. NO. OF PAGES 54
13. URL on the World Wide Web  <a href="http://www.dsto.defence.gov.au/corporate/reports/DSTO-RR-0231.pdf">http://www.dsto.defence.gov.au/corporate/reports/DSTO-RR-0231.pdf</a>		14. RELEASE AUTHORITY  Chief, Weapons Systems Division	
15. SECONDARY RELEASE STATEMENT OF THIS DOCUMENT  <i>Approved for public release</i>			
OVERSEAS ENQUIRIES OUTSIDE STATED LIMITATIONS SHOULD BE REFERRED THROUGH DOCUMENT EXCHANGE, PO BOX 1500, SALISBURY, SA 5108			
16. DELIBERATE ANNOUNCEMENT  No Limitations			
17. CASUAL ANNOUNCEMENT Yes 18. DEFTEST DESCRIPTORS			
Infrared detectors, Infrared tracking, Target acquisition, Antiship missiles, Sea skimming missiles, Scintillation, Infrared radiation			
19. ABSTRACT  As part of a study of the long range detection of antiship missiles (ASMs) by infrared search and track (IRST) systems using staring sensors, measurements of scintillation of an infrared source have been made. Scintillation of IR radiation from ASMs is one of a few features which may enhance ASM detectability by IRST systems. The measurements were made in the 3-5 micron band at ranges of 17 km and 19.9 km over water. The data were used to provide values for parameters of a phenomenological model of scintillation for use in development of detection algorithms. The parameters were the magnitude of irradiance, blurring effects and image location, and the correlation coefficients of these parameters. It was found that the probability distribution for the irradiance fluctuations was log-Gaussian, as predicted by theory. There was a temporal correlation for each of the parameters which was quantified by a correlation time, but none of the parameters were correlated with any other. Approximate methods were developed for correcting the data for the finite pixel size effects of the camera and the blurring effect of the optics.			